Morphogenesis in *Trypanosoma cruzi* epimastigotes proceeds via a highly asymmetric cell division

Paul C. Campbell[1] and Christopher L. de Graffenried[1,#]

1. Department of Molecular Microbiology and Immunology, Brown University, Providence, Rhode Island, USA;

[#]: Address correspondence to Christopher de Graffenried, christopher_degraffenried@brown.edu

ORCIDs: PCC: 0000-0003-3949-0062; CLdG: 0000-0003-3386-6487

Short title: *T. cruzi* morphogenesis during cell division

Abbreviations: FAZ: flagellum attachment zone, PTM: posttranslational modification, MT: microtubule. U-ExM: Ultrastructure expansion microscopy

Keywords: Cell division, *Trypanosoma cruzi*, Polo-like kinase, basal body, flagellum.

Abstract (246 words)

Trypanosoma cruzi is a protist parasite that is the causative agent of Chagas' disease, a neglected tropical disease endemic to the Americas. *T. cruzi* cells are highly polarized and undergo morphological changes as they cycle within their insect and mammalian hosts. Work on related trypanosomatids has described cell division mechanisms in several life-cycle stages and identified a set of essential morphogenic proteins that serve as markers for key events during trypanosomatid division. Here, we use Cas9-based tagging of morphogenic genes, live-cell imaging, and expansion microscopy to study the cell division mechanism of the insect-resident epimastigote form of *T. cruzi,* which represents an understudied trypanosomatid morphotype. We find that *T. cruzi* epimastigote cell division is highly asymmetric, producing one daughter cell that is significantly smaller than the other. Daughter cell division rates differ by 4.9 h, which may be a consequence of this size disparity. Many of the morphogenic proteins identified in *T. brucei* have altered localization patterns in *T. cruzi* epimastigoes, which may reflect fundamental differences in the cell division mechanism of this life cycle stage, which widens and shortens the cell body to accommodate the duplicated organelles and cleavage furrow rather than elongating the cell body along the long axis of the cell, as is the case in life-cycle stages that have been studied in *T. brucei*. This work provides a foundation for further investigations of *T. cruzi* cell division and shows that subtle differences in trypansomatid cell morphology can alter how these parasites divide.

Author Summary (165 words)

Trypanosoma cruzi causes Chagas' disease, which is among the most neglected of tropical diseases, affecting millions of people in South and Central America along with immigrant populations around the world. *T. cruzi* is related to other important pathogens such as *Trypanosoma brucei* and *Leishmania spp,* which have been the subject of molecular and cellular characterizations that have provided an understanding of how these organisms shape their cells and undergo division. Work in *T. cruzi* has lagged due to an absence of molecular tools for manipulating the parasite and the complexity of the original published genome; these issues have recently been resolved. Building on work in *T. brucei*, we have studied the localization of key cell cycle proteins and quantified changes in cell shape during division in an insect-resident form of *T. cruzi*. This work has uncovered unique adaptations to the cell division process in *T. cruzi* and provides insight into the range of mechanisms this family of important pathogens can employ to colonize their hosts.

Introduction

The Trypanosomatidae family encompasses parasitic species that inhabit a broad range of hosts including plants, insects, fish, and mammals[1–3]. These parasites tune core pathways including their metabolism and cell surface proteomes to survive within varied host environments[4–6]. Trypanosomatids have also adapted their cellular morphology to facilitate processes such as evasion of the host immune system, attachment to epithelial layers, and proliferation within host cells[7,8]. These morphological states have required adaptations to other essential cellular pathways such as cell division and endocytosis [9,10]. In recent years, work on the parasites *Trypanosoma brucei* and *Leishmania spp* has uncovered a range of trypanosomatid cell division mechanisms and identified key regulators, which include conserved eukaryotic proteins and trypanosomatid-specific components[10,11]. *Trypanosoma cruzi*, the causative agent of Chagas' disease, is a significant human health burden, with over 7 million chronic infections primarily in Latin America and 50,000 deaths annually[12]. The cellular biology of *T. cruzi* has not been studied as extensively as other trypanosomatids, primarily due to the complexity of the original sequenced genome and the lack of tools such as RNAi to probe essential gene function[13,14]. Recent genome sequencing of several *T. cruzi* strains and the development of Cas9 editing systems have remedied many of these problems [14–17].

Trypanosomatids share a set of organelles that facilitate infection and subsequent survival within their hosts[18]. As part of the Kinetoplastea class, trypanosomatids have a mitochondrial DNA aggregate known as the kinetoplast that duplicates asynchronously from the nucleus[1,19]. A single flagellum nucleates from a basal body docked to an invagination of the cell surface known as the flagellar pocket, which in some life-cycle

82 stages serves as a key endocytic and exocytic compartment that is crucial to host immune
83 evasion [9,20]. The flagellum traverses the pocket and then emerges onto the cell
84 surface. In some cases, the flagellum is attached laterally along the cell surface via a
85 series of junctional complexes known as the flagellum attachment zone (FAZ), while in
86 others the flagellum is detached from the cell surface [21,22]. Cells with free flagella still
87 retain a small FAZ segment near the neck of the flagellar pocket (**Fig 1**) [23]. A subset of
88 trypanosomatids have a separate tube-shaped endocytic membrane compartment
89 flanked by a set of cytoplasmic microtubules with an opening next to the flagellar pocket,
90 known as the cytostome-cytopharynx[24,25]. Nearly all trypanosomatids have a set of
91 subpellicular microtubules underlying the plasma membrane that persists throughout the
92 cell cycle and is responsible for shaping the cell body [26,27]. These microtubules are
93 heavily crosslinked to each other and to the plasma membrane.

94 Trypanosomatids assume a wide range of cell morphologies as they cycle within
95 their host environments. In the bloodstream of their vertebrate hosts, many
96 trypanosomatids assume a trypomastigote morphology, with the kinetoplast, flagellum,
97 and flagellar pocket on the posterior side of the nucleus, near the cell posterior [1,19].
98 The flagellum is attached to the plasma membrane by an extended FAZ. It has been
99 proposed that this morphology is optimized for motility in crowded, high-viscosity solutions
100 such as blood [28,29]. *T. brucei* and *T. cruzi* bloodstream forms assume a trypomastigote
101 morphology, while *Leishmania* assume a promastigote morphology, where the
102 kinetoplast, flagellar pocket, and minimally attached flagellum are on the anterior side of
103 the nucleus [30]. At certain locations within the insect host, *T. brucei* and *T. cruzi* adopt
104 an epimastigote morphology, with the kinetoplast and flagellum positioned on the anterior

105 side of the nucleus and a segment of attached flagellum extending towards the anterior
106 end of the cell [31–33]. This morphology is thought to be optimal for attachment to
107 epithelial surfaces, which is a common part of the insect infection stages (**Fig 1**).
108 Trypanosomatids remain polarized throughout their cell cycle, which has required
109 morphotypes to adapt the mechanisms used for duplicating and positioning organelles
110 during cell division to suit their specific needs [7].

111 In this work, we have studied the cell division of *T. cruzi* epimastigotes using
112 quantitative morphometrics and epitope-tagged proteins that are important cell cycle
113 components in *T. brucei*. We show that the epimastigote cell body widens and shortens
114 as it divides, suggesting that the cell division mechanism in this form is more similar to
115 the process in *Lieshmania* promastigotes. Epimastigote cell division appears highly
116 asymmetric, as the daughter cell inheriting the new flagellum is smaller than the old-
117 flagellum daughter. Using live-cell imaging, we show that the rate of daughter cell
118 divisions differs by nearly 5 h, which suggests that the asymmetry may result in one
119 daughter cell taking longer to complete a subsequent round of division. The construction
120 of a new posterior end recruits many of the cell cycle regulated proteins seen at the tip of
121 the new FAZ in *T. brucei*, along with tubulin posttranslational modifications usually
122 confined to the FAZ. These results provide a framework for describing the cell division
123 mechanism in the *T. cruzi* epimastigote, which is a common morphology found in many
124 trypanosomatids that has not been studied in detail previously.

125

126 **Results**

127 The cell division mechanism trypanosomatids employ is influenced by the
128 arrangement of the organelles within their specific morphotype [7]. The maturation of the
129 probasal body and assembly of the new flagellum are usually the earliest events, followed
130 by the assembly of a new FAZ, the duplication of the pocket and kinetoplast, and finally
131 nuclear duplication [10,34]. The subpellicular array must also be enlarged to
132 accommodate the duplicating organelles and to situate them within the cell body so that
133 cytokinesis will produce two daughter cells with the correct complement and arrangement
134 of organelles [35]. Cleavage furrow ingression initiates from the anterior end of the cell
135 body and moves towards the posterior end to complete cell division. In *T. brucei*
136 trypomastigotes, lengthening of the cell body is the primary means of accommodating
137 duplicated organelles and positioning them for inheritance; *Leishmania* promastigotes
138 widen their cell bodies while simultaneously shortening them [36,37]. It has been
139 speculated that the extended segment of attached flagellum in trypomastigotes may limit
140 their ability to widen their cell body, which has led to the lengthening mechanism [7]. The
141 *T. cruzi* epimastigote form, which has an attached flagellum like trypomastigotes but an
142 anterior-located flagellar pocket and kinetoplast, could provide insight into the effect of
143 flagellar attachment on cell division.

144 We employed Y-strain epimastigotes constitutively expressing *Streptococcus*
145 *pyogenes* Cas9 and T7 polymerase to tag genes at their native loci with three copies of
146 the Ty1 epitope fused to mNeonGreen, which allowed us to observe the native
147 fluorescence of the tagged protein or to employ anti-Ty1 antibodies for detection
148 [14,17,38–40]. We selected marker proteins based on recent work in *T. brucei* and
149 *Leishmania* that identified “landmark” proteins that provide bright signal as mNeonGreen

150 fusions for a range of cellular compartments [41]. For each protein, we tagged the
151 terminus that yielded the brightest signal based on the TrypTag whole-genome tagging
152 database [42]. The Cas9-T7 expressing epimastigotes were nucleofected with guide
153 DNAs containing a T7 promoter to produce a guide RNA targeting one terminus of the
154 gene of interest and a healing template that introduces the 3X-Ty1-mNeonGreen tag, an
155 intergenic region, and a selection marker. We tagged a series of proteins that localize to
156 the FAZ, extending new FAZ, basal body, and cell posterior in *T. brucei* trypomastigotes
157 to determine if their localization was similar in *T. cruzi* epimastigotes and to use these
158 marker proteins to study the mechanism of cell division in this morphotype.

159 We first observed the FAZ using 3X-Ty1-mNeonGreen::FAZ25 (TcYC6_0125610)
160 and the monoclonal antibody 1B41, which labels the FAZ in *T. brucei*. The 1B41 antibody
161 is thought to label a novel post-translational modification (PTM) of beta tubulin present in
162 the segment of the MtQ that is adjacent to the FAZ filament [43,44]. We noted that FAZ25
163 was present in a single thin structure underlying the flagellum, as would be expected for
164 the FAZ in epimastigote-form *T. cruzi* (**Fig 2**) [45]. The 1B41 signal generally colocalized
165 with FAZ25, but we observed additional 1B41-positive structures in dividing cells. Early
166 cell cycle cells containing one **N**ucleus and one **K**inetoplast (1N1K) could be separated
167 into two populations: smaller cells with a short FAZ and a separate 1B41 focus at the cell
168 posterior (**Fig 2A**), and larger cells with a longer FAZ and no posterior 1B41 labeling or a
169 much less intense signal than the shorter 1N1K cells (**Fig 2B**). Upon initiation of new FAZ
170 assembly, a small structure was observed in both the FAZ25 and 1B41 channels on the
171 ventral side of the old FAZ. The 1B41 punctum at the cell posterior, which was frequently
172 much brighter than the 1B41 signal at both the old and new FAZ, became visible at this

173 point (**Fig 2C, 2D**). In 2N2K cells with ingressing cleavage furrows, the posterior 1B41
174 punctum marked the last point of connection between the daughter cells (**Fig 2E**). The
175 new-flagellum daughter appeared to be significantly smaller than the old-flagellum
176 daughter in cells that were about to complete cytokinesis. Because of this asymmetry, we
177 propose that the small 1N1K cells with the bright 1B41 puncta are likely to be new-
178 flagellum daughter cells that have just completed cytokinesis. These smaller cells do not
179 appear to enter cell division in their current state, which suggests that they grow in size
180 and lose their 1B41 puncta over time prior to initiating cell division. The longer 1N1K cells
181 lacking the 1B41 puncta are likely to be a mixture of the old-flagellum daughter cells and
182 the new-flagellum daughter cells that have undergone subsequent growth after the
183 completion of cell division. This would also suggest that the 1B41 punctum is inherited
184 asymmetrically, with the new-flagellum daughter cell retaining the bulk of the signal (**Fig**
185 **3A**). This asymmetric inheritance is similar to what is observed in the partitioning of the
186 flagella connector in procyclic *T. brucei* cells, which allowed the definitive identification of
187 the new- and old-flagellum daughter cells after the completion of cell division [46].

188 The novel localization pattern of the 1B41 antibody in *T. cruzi* suggests that the
189 cell posterior is transiently modified with a tubulin PTM during cell division that is usually
190 confined to the MtQ segment adjacent to the FAZ filament *in T. brucei*. The posterior end
191 contains many of the plus ends of the subpellicular microtubules, which could be
192 specifically targeted by PTMs as part of the construction of the new cell posterior during
193 cell division [26]. We labeled *T. cruzi* with antibodies that detect tubulin tyrosination,
194 acetylation, and two forms of glutamylation to determine if they have similar labeling
195 patterns to 1B41 in dividing cells, which could indicate that they are labeling the same

196 tubulin PTM (**S1 Fig**). The YL1/2 antibody, which detects tyrosinated tubulin that is added
197 to growing microtubules, labeled the cell posterior, the posterior part of the subpellicular
198 array, and the basal body [47–49]. The GT335 antibody, which labels polyglutamate
199 chains of all lengths, and IN105, which labels polyglutamate chains at least three units in
200 length, both labeled the entirety of the subpellicular array, including the flagellum [50,51].
201 The 6-11B-1 antibody, which labels acetylated tubulin, labeled the entirety of the array
202 and the flagellum [52]. Considering the broad distribution of these antibody signals across
203 multiple structures that lack 1B41 signal, it is likely that the 1B41 epitope is not attributable
204 to tubulin tyrosination, acetylation, or glutamylation.

205 We performed a quantitative analysis of the cell cycle stages we established using
206 the localization patterns of FAZ25 and 1B41 to measure how *T. cruzi* changes as it
207 divides. We employed a statistical method that relies on an asynchronously dividing
208 culture to establish the length of time that cells spend in different states [53,54]. This
209 approach relies on a precise measurement of parasite doubling time, which we assessed
210 for our Cas9-T7 cell line over the course of 9 d. We found a persistent doubling time of
211 22.1 h, which we used along with the number of cells in each of our FAZ25/1B41
212 categories to define the epimastigote cell cycle (**Fig 3B and 3C**). *T. cruzi* epimastigotes
213 spend 80% of their time as one **N**ucleus, one **K**inetoplast, and one **F**lagellum (1N1K1F)
214 cells, representing 17.6 h of the cell cycle. New- and old-flagellum daughter cells
215 containing the 1B41 posterior puncta account for 6% and 4.4% of the cell population,
216 respectively (**Fig 3C**). New flagellum and FAZ growth initiates from a point on the ventral
217 side of the cell next to the existing FAZ and flagellum. The 1B41 puncta appears at this
218 time as well. The briefest window of the cell cycle occurs after kinetoplast duplication and

219 prior to nuclear duplication (1N2K), which represents just under 30 min. It should be noted
220 that at this stage the *T. cruzi* kinetoplasts label brightly with DAPI and are in close
221 proximity to one another, making it difficult to clearly determine when the cells reach the
222 2K state. Consequently, the number of cells we identified as 1N2K2F, and therefore the
223 length of time the cells spend in this state, is likely an underestimate. *T. cruzi* spends
224 considerably longer in the 2N2K2F stage; almost all of these cells have an ingressing
225 cleavage furrow, which suggests that cytokinesis initiates rapidly after the completion of
226 karyokinesis (**Fig 3D**).

227 We also monitored the morphologic changes that occur in epimastigotes as they
228 divide. We measured the width of the cell along its shortest axis and the overall cell length
229 including the extension of the flagellum and the cell body alone. We also measured the
230 distances between the cell posterior and the kinetoplast and nucleus, along with the
231 lengths of the flagellum and FAZ (**Fig 4A**). We noted that the cell body length and the
232 distances between the nucleus and kinetoplast and the posterior end of the cell decline
233 towards the end of cell division while the overall width of the cell body increases (**Fig 4B-**
234 **E, 4H**). The cell body shortening seems to be restricted to the cell posterior as the old
235 FAZ and flagellum lengths remain unchanged (**Fig 4F and 4E**). The cells that we
236 previously identified as small with a bright 1B41 punctum at their cell posteriors were
237 shorter than 1N1K1F cells lacking puncta or with weak puncta labeling, which suggests
238 that the new-flagellum daughter cells are significantly shorter than the old-flagellum
239 daughter cells right after completing cytokinesis.

240 We focused on the difference between the new and old FAZ and flagellum lengths
241 as an indicator of the asymmetry present during the late stages of cell division (**Fig 5A**).

242 The new FAZ averages 2.2 microns in cells that are undergoing cytokinesis, while the old
243 FAZ remains approximately 12 microns long throughout cell division, showing the
244 extreme asymmetry between the inherited structures (**Fig 4F and 5B**). The difference
245 between the length of the old and new flagella was smaller, with new flagellum lengths at
246 the latest stages of cell division reaching 9 microns, compared to 18 microns for the old
247 flagellum (**Fig 4G and 5C**). This result strongly suggests that most of the asymmetry
248 observed during *T. cruzi* epimastigote cell division is attributable to the construction of a
249 smaller new cell body that is inherited by the new flagellum/FAZ daughter. The new
250 flagellum daughter cell must then increase its cell body length and extend the FAZ prior
251 to initiating another round of cell division (**Fig 5D and 5E**).

252 We labeled the parental Y-strain *T. cruzi* line with 1B41 and quantitated its cell
253 morphology to confirm that the posterior punctum 1B41 signal and the asymmetric cell
254 division we observed was not due to the presence of Cas9 and T7 polymerase in our
255 tagging cell line. We found that the parental strain also has the posterior 1B41 signal and
256 widens and shortens over the course of cell division (**S2 Fig**). We also noted the
257 asymmetry between the new flagellum and old flagellum daughter cells during the late
258 stages of cytokinesis, and that 1N1K cells with the posterior 1B41 punctum were
259 significantly smaller than 1N1K lacking the punctum. We also labeled Brazil A4 strain *T.*
260 *cruzi* epimastigotes with 1B41 and saw the posterior punctum and asymmetry in the
261 daughter cells during division, which suggests that these features are generally
262 conserved among different *T. cruzi* strains.

263 We next tagged the protein SAS-6 (TcYC6_0070700) to gain insight into the basal
264 body duplication cycle in *T. cruzi*. In *T. brucei*, TbSAS-6 is present at both the pro and

265 mature basal body throughout cell division [55,56]. We tagged TcSAS-6 with 3X-Ty1-
266 mNeonGreen and followed its localization over the cell cycle with 1B41 as a colabel (**Fig**
267 **6**). TcSAS-6 labels both the pro and mature basal body in 1N1K1F cells containing the
268 posterior 1B41 puncta, denoting cells that had just recently completed cell division.
269 Curiously, we noted in 1N1K cells that had produced a new flagellum (arrowhead) and
270 were developing a new 1B41 punctum still only had two TcSAS-6-positive structures. In
271 *T. brucei*, cells with two flagella have four TbSAS-6-positive structures, reflecting two
272 pairs of pro and mature basal bodies. At later points in cell division, we noted cells with 3
273 and 4 TcSAS-6-positive structures, suggesting that SAS-6 is eventually incorporated into
274 all of the basal bodies (**Fig 6A**). We used the pan-centrin antibody 20H5 as another
275 marker that should persistently label both the pro and mature basal body [57]. In cells
276 colabeled for TcSAS-6, we were able to observe 20H5-positive basal bodies at the base
277 of the flagella in dividing cells that lacked SAS-6 labeling, showing that the absence of
278 TcSAS-6 did not impact other persistent basal body markers (**S3A Fig**). As another
279 control, we looked at the intrinsic fluorescence of the mNeonGreen appended to TcSAS-
280 6 to make sure that antibody accessibility was not limiting our ability to detect all the SAS-
281 6 present in the cell. The mNeonGreen fluorescence followed the same pattern as
282 observed by immunofluorescence (**S3B Fig**).

283 We employed ultrastructure expansion microscopy (U-ExM) coupled with SoRa
284 super-resolution imaging to better characterize the localization pattern of TcSAS-6 in *T.*
285 *cruzi* (**Fig 6B**) [58–60]. U-ExM provides an approximately 5-fold enhancement in
286 resolution that is further enhanced by $\sqrt{2}$ past the light limit with SoRA, which also
287 provides confocal sectioning [61]. We used anti-Ty1 labeling for TcSAS-6 and the TAT1

288 anti-tubulin antibody to label the flagellum, basal body, the microtubules associated with
289 the cytostome, and subpellicular array [62]. In the expanded samples, we were able to
290 clearly identify pro and mature basal bodies at all stages of cell division. We observed
291 TcSAS-6 labeling of both the pro and mature basal body in cells with a single flagellum.
292 In cells that had just begun to duplicate the basal body, which can be identified by the
293 rotation of the maturing probasal body to facilitate docking with the flagellar pocket
294 membrane, the two TcSAS-6 puncta were no longer associated with the barrel of the pro
295 or mature basal body, but appeared to be adjacent in two discrete foci. There were still
296 two SAS-6 puncta associated with the duplicated basal bodies in cells that had begun to
297 divide that contained a short new flagellum, but the puncta were found exclusively on both
298 probasal bodies. There was no TcSAS-6 signal on the mature basal bodies that nucleated
299 the old and new flagella. At later stages of cell division, which we could identify by the
300 increased length of the new flagellum, we could observe SAS-6 signal restored to the
301 mature basal bodies, which is consistent with our immunofluorescence results (**Fig 6B**).
302 With the additional resolution provided by U-ExM and SoRa imaging, we noted that the
303 TcSAS-6 signal on the probasal body is actually two distinct puncta at this stage of cell
304 division, one that appears to be associated with the base of the probasal body and
305 another punctum on the side of the probasal body at the approximate midpoint of the
306 structure. These results suggest that SAS-6 levels decline significantly at the mature
307 basal body in *T. cruzi* during cell division and that this decline may be linked to basal body
308 duplication.

309 Proteins that transiently localize to the tip of the extending new FAZ play an
310 essential role in positioning the cleavage furrow in *T. brucei* trypomastigotes [10]. Several

311 cytokinetic proteins are present at the tip of the new FAZ in *T. brucei* trypomastigotes and
312 are thought to use its extension and position within the cell body to guide the placement
313 of the new cell anterior and designate the starting point for cleavage furrow ingression.
314 Among these proteins is the cytokinetic scaffolding protein TbTOEFAZ1 (also known as
315 TbCIF1), which is essential for cleavage furrow placement in *T. brucei* cells [63,64]. We
316 tagged the *T. cruzi* homolog of TcTOEFAZ1 (TcYC6_0051010) and monitored its
317 localization. In *T. brucei*, TbTOEFAZ1 expression is found at the tip of the extending new
318 FAZ and then along the cleavage furrow. In *T. cruzi*, we noted that all cells, regardless of
319 cell cycle stage, expressed TcTOEFAZ1 (**Fig 7**). In the early stages of the cell cycle prior
320 to new FAZ assembly, TcTOEFAZ1 was localized to a short bar-like structure adjacent to
321 the proximal end of the old FAZ. This localization is similar to the position of the new FAZ
322 that appears during the later stages of cell division. In cells that had begun to assemble
323 the new FAZ, TcTOEFAZ1 localized along the length of the new structure, but did not
324 form a focus at the tip as it does in *T. brucei*. TcTOEFAZ1 is also present at the point
325 where the cleavage furrow ingresses in *T. cruzi*, which is found between the two flagella
326 (**Fig 7A**).

327 We employed U-ExM and SoRa imaging to further establish the localization of
328 TcTOEFAZ1, using anti-tubulin as a colabel (**Fig 7B**). In early cell cycle cells,
329 TcTOEFAZ1 localized to a structure on the ventral side of the new flagellum, along with
330 a small amount of labeling underlying the segment of the old flagellum just as it exits the
331 flagellar pocket. In dividing cells, TcTOEFAZ1 localization appeared to encircle the point
332 where the new flagellum exits the flagellar pocket onto the cell surface. TcTOEFAZ1 was
333 present at the position of the ingressing furrow, in the area between the new and old

334 flagellum. We were unable to directly compare TcTOEFAZ1 localization to a FAZ marker
335 because U-ExM imaging does not appear to preserve sufficient signal for 1B41 or FAZ25.
336 The Polo-like kinase (TbPLK) homolog present in *T. brucei* binds to and
337 phosphorylates TbTOEFAZ1, which is essential for TbPLK localization to the tip of the
338 extending FAZ [65,66]. Recently, a second homolog of TbPLK has been identified in *T.*
339 *brucei*, but little is known about its function [67]. We tagged the TbPLK1 homolog in *T.*
340 *cruzi* to compare its localization pattern to the *T. brucei* homolog (**Fig 8A**). TcPLK1
341 (TcYC6_0047790) was not expressed in cells early in the cell cycle, which is consistent
342 with TbPLK expression patterns in *T. brucei*. During the early stages of cell division
343 TcPLK1 initially localized to the basal body, as is the case during *T. brucei* cell division
344 [68]. However, the kinase does not subsequently collect at the tip of the new FAZ, but
345 rather localizes along the length of the old FAZ. TcPLK1 also localizes to the new FAZ
346 once this structure becomes visible. TcPLK1 is subsequently present at the cell posterior,
347 appearing just prior to the 1B41-positive puncta, then colocalizing with it, which
348 represents a novel localization pattern for the kinase in trypanosomatids. TcPLK1 does
349 not appear to track along the cleavage furrow during the latest stages of cell division,
350 which is consistent with its localization in *T. brucei* trypomastigotes (**Fig 8A**).
351 In *T. brucei,* the orphan kinesin TbKLIF plays an important role in the last stages
352 of cell division during the construction of a new cell posterior [69–71]. In *T. cruzi*, 3X-Ty1-
353 mNeonGreen::TcKLIF (TcYC6_0055740) colocalized with the 1B41 posterior puncta in
354 cells that had recently completed cell division (**Fig 8B**). 1N1K cells lacking the puncta no
355 longer had KLIF signal, suggesting that KLIF is downregulated during the early stages of
356 the cell cycle. Once the cells had begun to divide, we were able to observe weak

357 expression of TcKLIF along the FAZ, followed by localization to the new FAZ and the
358 posterior puncta in cells at later cell cycle stages. In cells undergoing cytokinesis, TcKLIF
359 no longer localized to the FAZ but instead was clearly associated with the position of the
360 ingressing furrow. At the latest stages of cell division, TcKLIF localized to two discrete
361 foci at the cell posterior that appeared to be subdomains of the 1B41 punctum (**Fig 8B**).
362 This argues that the 1B41-positive punctum may represent a microtubule-containing
363 structure that replicates during the last stages of cell division, perhaps to facilitate the
364 construction of a new posterior end. The levels of TcPLK1 and TcKLIF signal were not
365 sufficient for U-ExM analysis, which creates a 125-fold decline in fluor density.

366 Considering the size difference between the two daughter cells produced during
367 *T. cruzi* epimastigote cell division, it is possible that there would be a difference in their
368 cell division rates during their subsequent round of division. We recently developed a
369 strategy using agarose microwells that allows us to confine and image trypanosomatids
370 in small volumes without immobilization, which permits the parasites to divide at rates
371 similar to those in bulk cultures [72]. During optimization of our microwell approach for
372 imaging *T. cruzi* epimastigotes, we found that increasing the height of the wells to 6
373 microns to account for the width of *T. cruzi* epimastigote cells undergoing cytokinesis
374 provided unimpeded cell divisions, with no loss in viability out to 48 h. We isolated single
375 cells in wells and monitored them until they divided, then tracked the subsequent division
376 rate of the daughter cells (**Fig 9A and S1 Movie**). Cells divided in the microwells at a
377 faster rate than in bulk cultures, with an average rate of 15.4 h for all the events we
378 observed, compared to 22.1 h in culture. This increased rate may reflect the fact that the
379 agarose microwells do not exchange gas with the environment, which would lead to

380 decreased oxygen levels within the well over time. Recent work has shown that *T. cruzi*
381 epimatigotes grow more rapidly in anoxic environments, which is consistent with the
382 conditions within the insect gut that they inhabit throughout their time within this host [73].
383 We found that there was a 4.9 h difference in the rates of daughter cell divisions in
384 epimastigote *T. cruzi,* with the median first division occurring at 12.8 h and the second
385 division occurring at 17.7 h (**Fig 9B and 9C**). This difference is larger than what we
386 observed in *T. brucei*, which suggests that the increased asymmetry in *T. cruzi*
387 epimastigote cell division leads to a larger difference in daughter cell division rate.
388

389 **Discussion**

390 In this work, we have studied *Trypanosoma cruzi* epimastigote cell division using *T. cruzi*
391 gene editing and components of the parasite cell division apparatus and cytoskeleton that
392 were identified in localization studies conducted in other trypanosomatids. These
393 advances have allowed us to define different *T. cruzi* cell cycle stages based on cell
394 morphology and the localization of marker proteins for comparison with previous work on
395 promastigote *Leishmania* and trypomastigote *T. brucei* stages. Of these four
396 trypanosomatid forms, epimastigote *T. cruzi* appears to have the most asymmetric cell
397 division mechanism, producing a new-flagellum daughter cell only half the length of the
398 old-flagellum daughter cell body. We observed a significant difference in the division rates
399 of the two daughter cells in agarose microwells, which argues that this asymmetry impacts
400 the duration of the subsequent round of cell division. Most of the cytoskeletal and cell-
401 division proteins we studied have altered localization patterns compared to what is
402 observed in *T. brucei* (**Fig 10**). The tip of the growing new FAZ, which recruits many

403 essential cytokinetic proteins such as such as TbTOEFAZ1, TbKLIF, and TbPLK in *T.*
404 *brucei* does not function as their primary localization point in *T. cruzi.* These proteins
405 appear to localize along the lengths of the old and new FAZ. The posterior end of the cell
406 recruits many of these cytokinetic proteins and may contain tubulin posttranslational
407 modifications that are confined to the FAZ in *T. brucei*. These changes likely reflect the
408 differing geometries that *T. brucei* trypomastigote and *T. cruzi* epimastigote cells adopt
409 during cell division, which put unique constraints on the timing and positioning of
410 duplicating organelles.

411 Work that predates the development of Cas9 editing in *T. cruzi* examined different
412 aspects of the epimastigote cell cycle, with an emphasis on flagellar pocket and nuclear
413 duplication [74], noted that the new flagellum appeared significantly shorter than the old
414 during the later stages of cell division. One point of difference is that the authors state
415 that the new flagellum length reaches near parity with the old flagellum prior to the
416 completion of cell division. In our experiments, the asymmetry present during the later
417 stages of cell division is carried on to the daughter cells, with the new-flagellum daughter
418 having a significantly shorter new flagellum and FAZ.

419 Labeling with the 1B41 antibody provides a useful method for tracking division in
420 *T. cruzi*. While the specific epitope of the antibody is still unknown, it appears to be a PTM
421 of beta tubulin. *T. cruzi* cells contain several MT structures that likely derived from the MT
422 rootlets found in the feeding apparatus of the free-living ancestor of the trypanosomatids,
423 including a second MT quartet and a MT triplet associated with the cytopharynx [24,25].
424 None of these MT structures appear to label with 1B41, suggesting that the FAZ-
425 associated MtQ is uniquely modified. It is currently unknown why the 1B41 signal

426 partitions into the daughter cells asymmetrically, but it may reflect differences in the PTM
427 status of certain microtubule plus ends that selects them for incorporation into the new-
428 flagellum daughter cell posterior, while leaving the less-modified plus ends in the old
429 structure. It is possible that the 1B41 epitope facilitates recruitment of the proteins
430 responsible for duplicating the cell posterior. TcPLK localizes to the cell posterior just prior
431 to the appearance of the 1B41 signal, so the kinase may function as an upstream
432 regulator of this process. KLIF localizes to the cell posterior during late cytokinesis and
433 appears to resolve into two distinct foci, which suggests that the kinesin may be
434 responsible for sorting the MT plus ends into two discrete structures to complete
435 cytokinesis. This is consistent with the proposed function of KLIF in *T. brucei*, where
436 depletion of the motor leads to a block in assembly of a new cell posterior and
437 subsequently prevents cell division [69,70]. In trypomastigotes, formation of a new cell
438 posterior occurs de novo at a location which initially appears as a new focus of MT plus
439 ends that are subsequently gathered into a MT bundle to complete cell division [36]. In
440 epimastigotes, it appears that cell posterior assembly occurs at the site of the old posterior
441 and may involve the addition of MTs, followed by partitioning of the duplicated structure.
442 A previous survey of trypansomatid morphologies has suggested that cells with
443 detached flagella, termed “liberforms”, tend to undergo cell widening during cell division,
444 whereas cells with attached flagella, termed “juxtaforms” lengthen their cells as they
445 divide [7]. It was suggested that epimastigotes, which are juxtaforms, may employ a more
446 trypomastigote-like mechanism for cell division. Our results with *T. cruzi* suggest that
447 epimastigotes actually employ a liberform-like division mechanism. However, limiting the
448 length of the new FAZ, which would create a significant impediment to altering the shape

449 of the cell body, may be necessary to widen the cell. This may explain the extreme
450 asymmetry of cell division in epimastigote *T. cruzi*.

451 In *T. brucei*, the tip of the new extending FAZ plays an important role in designating
452 the point of cleavage furrow ingression [11]. The tip is in close proximity to the old FAZ
453 and contains a host of proteins that are thought to play a role in triggering cytokinesis,
454 including the CIFs, TOEFAZ1, KLIF, and PLK. In *T. cruzi* epimastigotes, PLK localizes
455 along the old and new FAZ prior to moving to the cell posterior, while KLIF localizes to
456 both FAZ, then the cell posterior, followed by the cleavage furrow. While both of these
457 proteins remain cell-cycle regulated, TOEFAZ1 appears to be persistently expressed,
458 initially localizing to a position similar to where the new FAZ is assembled, then moving
459 along the ingressing furrow. In trypomastigote *T. brucei*, the extension of the new
460 flagellum and FAZ are tightly coordinated, with the FAZ extending 1-2 microns behind the
461 flagellum [75]. In *T. cruzi* epimastigotes, FAZ and flagellar growth are not tightly coupled,
462 as the new flagellum extends far beyond the end of the new FAZ. It is possible that using
463 the tip of the new FAZ to target the cytokinetic complex may be a feature exclusive to
464 cells with trypomastigote morphology.

465 The basal body protein TcSAS-6 appears to have a different localization pattern in
466 *T. cruzi* compared to other trypanosomatids. The protein is one of the earliest components
467 of the probasal body and is thought to establish the 9-fold symmetry of the organelle by
468 constructing a cartwheel-shaped structure at its base [55,76,77]. In *T. brucei*, depletion
469 of TbSAS-6 causes defects in probasal body assembly and blocks the production of a
470 new flagellum, causing growth arrest [56]. In some organisms, the cartwheel structure
471 breaks down during the completion of cell division, which leads to a loss in SAS-6 signal,

472 although the cartwheel remains as a persistent component of the basal body in many
473 organisms including *T. brucei* [78]. In *T. cruzi*, TcSAS-6 is present at the pro and mature
474 basal body early in the cell cycle, then moves to the bases of the assembling probasal
475 bodies. It then is restored to the mature basal bodies prior to cytokinesis while remaining
476 associated with the probasal bodies. This inheritance pattern is consistent with the
477 function of SAS-6 in probasal body assembly and may suggest that the new cartwheel is
478 assembled on the basal and probasal bodies after their duplication but prior to the
479 completion of cell division, so that the new probasal bodies can be assembled during the
480 subsequent round of division. While this would be different than what is observed in *T.*
481 *brucei*, earlier reports have shown that TbSAS-6 levels on the basal body fluctuate during
482 cell division, with higher levels in the probasal body during its assembly [79].

483 Our localization and morphology studies have highlighted significant differences in
484 *T. cruzi* epimastigote cell division compared to previously studied trypanosomatids. The
485 next step will be to determine if the changes in localization of proteins such as TcPLK and
486 TcKLIF reflect changes in their function. While knockout strategies are available in *T.*
487 *cruzi*, methods for targeting essential genes using conditional or inducible approaches
488 are still under development. It would also be interesting to localize these proteins in *T.*
489 *brucei* epimastigotes to determine if they retain the localization pattern seen in
490 trypomastigotes or if their morphotype alters the patterns. Currently, *T. brucei*
491 epimastigotes can only be isolated directly from the insect host [31,33]. As the ancestral
492 trypanosomatid likely had a promastigote-like morphology, its cell division mechanism
493 served as a starting point for diversification as organisms moved into new hosts [80]. The
494 trypomastigote form appears to be primarily an adaptation to survival within the

495 bloodstream of vertebrate hosts, which has made it a focus of much of the previous work
496 on trypanosomatids. However, with a better understanding of the range of morphologies
497 present among these organisms and the tools for sequencing and manipulating them, a
498 broader understanding of their cell division pathways is now feasible.

Acknowledgements

We would like to thank Rick Tarleton for providing *T. cruzi* cells, Martin Taylor for the Cas9-pLEW13 vector, Jack Sunter for the TAT1 antibody, and Kate O'Connor Giles and the Carney Institute of Brain Science for access to the Nikon SoRa microscope. We would also like to thank Sue Vaughan and Drew Etheridge for valuable insights. The research reported in this publication was supported by NIAID-NIH under awards R01AI166363 and R21AI151490 to CLdG. The content is solely the responsibility of the authors and does not necessarily represent the official views of the National Institutes of Health.

510 **Materials and methods**

511 **Cell culture and growth curves**

512 Cells used for all experiments were *T. cruzi* Y strain epimastigotes were cultured in LDNT
513 medium (0.5% Oxoid neutralized liver digest (ThermoFisher Scientific, Waltham, MA), 68
514 mM sodium chloride (ThermoFisher Scientific), 70 mM Tryptone (ThermoFisher
515 Scientific), 5 mM potassium chloride (ThermoFisher Scientific), 58 mM sodium phosphate
516 dibasic (ThermoFisher Scientific), 11 mM glucose (ThermoFisher Scientific), 25 μM
517 Hemin (Sigma-Aldrich, St. Louis, MO), gentamicin (25 μg/mL) (ThermoFisher Scientific),
518 10% heat inactivated fetal bovine serum (Bio-Techne), penicillin-streptomycin (100U/mL)
519 (ThermoFisher Scientific), pH 7.2) at 27 °C. For selecting cell lines, blasticidin was used
520 at 100 μg/mL and G418 at 500 μg/mL. Cell counts were obtained with a Z2 Coulter
521 Counter (Beckman Coulter, Brea, CA). Growth curves were performed in triplicate
522 seeding a culture of cells at 2×10^6 cells/mL. Cell counts were obtained every 24 h for 9 d
523 with reseeding 2×10^6 cells/mL into fresh flasks and media every 3 d.

524

525 **Calculation of cell cycle timing**

526 In order to calculate relative time spent in each cell cycle intermediate, a method
527 previously described [37,54]was employed to account for an asynchronous logarithmic
528 culture growth of cells that divide by binary fission with the equation:

529 $$x = t\frac{\ln\left(1-\frac{1}{2}y\right)}{-\ln(2)}$$

530 In this equation, x= the time through the cell cycle, y= proportion of cells preceding and
531 including the cell cycle stage in question, and t= cell cycle length.

532

533 **Cloning and cell line assembly**

534 Cas9 and T7 RNA polymerase expressing cells were generating using a pLEW13-Cas9
535 plasmid provided by Martin Taylor (London School of Hygiene and Tropical Medicine,
536 London, United Kingdom) as previously described [17]. Healing constructs for gene
537 tagging were generated by PCR using gene-specific primers with 30 bp homology
538 flanking the CRISPR-Cas9 cut site. A base plasmid containing a blasticidin resistance
539 marker, an intergenic sequence isolated from *T. brucei*, and a 3×Ty1 epitope tag fused to
540 a mNeonGreen fluorescent protein was employed as a template for PCR to generate all
541 healing constructs All proteins studied here were tagged as closely to the N-terminus as
542 allowed by available CRISPR-Cas9 cut sites. PCRs to generate the healing constructs
543 were performed in triplicate, pooled and purified with a Zymo Research DNA Clean and
544 Concentrator kit (Genesee Scientific, San Diego, CA) and resuspended in 25 µL of ultra-
545 pure water (Genesee).

546

547 sgRNAs were prepared with a gene specific forward primer with target site determined by
548 Eukaryotic Pathogen CRISPR guide RNA/DNA Design tool (http://grna.ctegd.uga.edu/)
549 using the *T. cruzi* Y C6 Pacbio genome assembly [14,15]. sgRNA was amplified in
550 triplicate as previously described[81]. sgRNA PCRs were pooled and purified with a Zymo
551 Research DNA Clean and Concentrator kit (Genesee Scientific) and resuspended in 25
552 µL of Ultra-Pure Water (Genesee). Purified sgRNA was pooled with corresponding
553 purified healing template for a total of 50 µL. Primers used in this study can be found in
554 S1 Table.

555

556 5×10^7 cells expressing SpCas9 and T7 RNA polymerase from a logarithmically growing
557 culture were harvested by centrifugation at 800×g for 5 min at 4 °C. Cells were
558 resuspended in 225 µL nucleofection buffer (90 mM sodium phosphate dibasic, 5 mM
559 potassium chloride, 0.15 mM calcium chloride hexahydrate, 50 mM HEPES). Pooled
560 sgRNA and healing template were added to the cell suspension and nucleofected using
561 a Lonza Nucleofector 2b (Lonza, Basel, Switzerland) using program X-014. Cells were
562 added to 10 mL LDNT media without selection markers. 24 h post nucleofection, selection
563 marker was added to the cells. Once a polyclonal bulk culture was established, cells were
564 plated for clonality by serial dilution.
565
566 **Immunofluorescence**
567 Cells were fixed in media with an equivalent volume of 8% PFA in PBS (4% final
568 concentration) for 20 min at RT. Cells were then centrifuged at 800×g for 5 min at RT and
569 washed once in 1 mL of PBS. Cells were centrifuged onto coverslips at 800×g for 5 min
570 4 °C. Coverslips were then inverted onto a solution of 0.5% NP-40 in PBS for 5 min,
571 followed by 3×5 min washes in PBS. Cells were incubated in blocking buffer (5% goat
572 serum (Gibco, ThermoFisher Scientific, Waltham, MA) in PBS) followed by 3×5 min
573 washes in PBS. Coverslips were incubated in primary antibody in blocking buffer for 1 h
574 at RT followed by 3×5 min washes in PBS. Coverslips were then incubated in secondary
575 antibody in blocking buffer for 1 h at RT followed by 3×5 min washes in PBS and then
576 mounted in Fluoromount G with DAPI (Southern Biotech, Birmingham, AL).
577
578 **Ultrastructure expansion sample preparation**

579 $1x10^6$ cells per gel were fixed in solution by adding 2X fixative solution (1.4% PFA, 2%
580 Acrylamide, 2X PBS) 1:1 to cells in media. Cells were spun 1000×g for 10 min at RT.
581 Cells were resuspended in 750 µL 1X fixative solution (0.7% PFA, 1% acrylamide, 1X
582 PBS) and spun again 1000×g for 10 min at RT. Cells were resuspended in 500 µL of 1X
583 fixative solution and spun down onto 12 mm coverslips by briefly centrifuging at 800×g at
584 4 °C. Coverslips were inverted onto 100 µL of 1X fixative solution in a humidified chamber
585 and incubated at 37 °C for 3.5 h. Slips were inverted onto 40 µL of gelation solution (19%
586 sodium acrylate, 10% acrylamide, 2% Bis, 1×PBS). 40 µL of fresh gelation solution was
587 added to 0.5 mL centrifuge tubes. 2 µL of 10% tetramethylethylendiamine (TEMED),
588 followed by 2 µL of ammonium persulfate (APS) were added to the 40 µL gelation solution
589 to initiate polymerization. The tube was vortexed briefly, then the solution was pipetted
590 onto 18 mm coverslips. Cells on 12 mm coverslips were then inverted onto the activated
591 gelation solution. Slips were placed at 37 °C to fully polymerize for 1 h in a 12 well plate.
592 1.5 mL denaturation buffer (200 mM SDS, 200 mM NaCl, 50 mM Tris) was added to the
593 wells and placed on a rocker at RT for 15 min. Gels were removed from cover slips and
594 placed in a 1.5 mL tube with 1 mL denaturation buffer. Gels were denatured at 95 °C for
595 30 min. Gels were poured into 150 mm petri dishes filled with DI water and allowed to
596 expand for 30 min at RT. Water was exchanged for fresh DI water and allowed to expand
597 overnight. The next day, gels were shrunk in 1X PBS for 30 min. Gels were transferred
598 to a 6 well plate and 300 µL of primary antibody in blocking buffer (2% BSA in 1X PBS)
599 was added and allowed to incubate on a rocker for 8 h. Gels were washed 3×10 min in
600 PBS-Tween on a rocker. 300 µL of secondary antibody in blocking buffer was added and
601 allowed to incubate at 37 °C with gentle agitation overnight. Gels were washed 3×10 min

602 in PBS-Tween on rocker. Gels were then re-expanded in DI water with 2 water changes
603 every 30 min. Next day, a 10 mm diameter gel slice was excised and placed in a MatTek
604 35 mm dish, No. 1.5 Coverslip, 10 mm Glass Diameter (MatTek Corporation, Ashland,
605 MA) coated with Poly-D-Lysine (Thermo Fisher Scientific) for imaging.
606
607 **Antibodies**
608 The following primary antibodies and dilutions were used in these experiments: anti-Ty1
609 (1:1,000 for IF and western blotting, 1:10 for U-ExM) from Sebastian Lourido
610 (Massachusetts Institute of Technology, Boston, MA), 1B41 (1:1,000 for IF) from Linda
611 Kohl (Centre National de la Recherche Scientifique, Paris, France), TAT1 (1:10,000 for
612 IF, 1:100 for U-ExM) from Jack Sunter (Oxford Brookes University, Oxford, United
613 Kingdom), anti-polyglutamylation GT335 (1:25,000 for IF) (Adipogen, San Diego, CA),
614 anti-polyglutamate chain IN105 (1:10,000 for IF) (Adipogen), 20H5 (1:1000 for IF) from
615 EMD Millipore.
616
617 Secondary antibodies were used in these experiments. All dilutions for IF were 1:1000,
618 U-ExM were 1:100, and western blotting were 1:10,000. Goat anti-mouse IgG1 Alexa
619 Fluor 488 (Thermo Scientific), Goat anti-mouse IgM Alexa Fluor 488 (Thermo Scientific),
620 Goat anti-mouse IgG2a Alexa Fluor 568 (Thermo Scientific), Goat anti-rat IgG H&L Alexa
621 Fluor 568 (Thermo Scientific), Goat anti-rabbit IgG Alexa Fluor 568, Goat anti-mouse IgG
622 (H&L) HRP (Thermo Scientific).
623
624 **Immunofluorescence microscopy**

625 IF images were obtained on a Zeiss Axio Observer Z1 microscope (Carl Zeiss
626 Microscopy, Oberkochen, Germany) using a 100×/1.4 NA Plan Aprochromat objective
627 lens. Images were captured using an ORCA-Flash 4.0 V2 sCMOS camara (Hamamatsu,
628 Shizouka, Japan) with Slidebook 6 microscopy software (Intelligent Imaging Innovations
629 Inc.)
630
631 **SoRa microscopy**
632 Ultrastructure expansion gels were imaged on a Nikon Eclipse Ti2 microscope (Nikon
633 Instruments, Melville, NY) equipped with a Yokogawa CSU-W1 SoRa super resolution
634 confocal scanning unit (CSU-W1, Yokogawa Electric, Musashino, Japan) and a
635 Photometrics Prime BSI sCMOS camera (Teledyne Photometrics, Tucson, AZ) using a
636 CFI APO TIRF 60× 1.49 oil objective (Nikon Instruments). Images were taken as a z-
637 stack at 0.1 μm per step. Images were denoised using Nikon NIS-elements software and
638 deconvoluted using Richardson-Lucy deconvolution.
639
640 **Generating agarose microwells**
641 PDMS stamps and agarose microwells were fabricated as previously described, for a final
642 concentration of 3.5% SeaPlaque agarose (Lonza, Basel, Switzerland) in LDNT media
643 [72]. Microwell dimensions used in these studies were 50×50×6 μm. Prepared agarose
644 grids were stored at 4 °C for up to one week with sufficient LDNT media to prevent drying
645 out.
646
647 **Live cell plating and imaging**

648 1 mL of *T. cruzi* cells expressing Cas9 and the T7 polymerase at 1×10^7 cells/mL density
649 were centrifuged at 800×g for 5 min at RT. Cells were resuspended in 1 mL fresh LDNT
650 media with 100 μM reduced L-glutathione (Sigma-Aldrich, St. Louis, MO). 125 μL of cells
651 containing 1.25×10^6 cells were plated in a Lab-Tek II chambered coverglass #1.5
652 Borosilicate chamber (Nunc International, Rochester, NY). A cut-to-fit agarose grid was
653 inverted onto the cells and the chamber sealed as previously described. Imaging chamber
654 was placed into a live-cell imaging insert (Oko labs) set to 27 °C and mounted on a Zeiss
655 Axio Observer Z1 microscope using a 20×/0.8 NA Plan Aprochromat objective lens. Cells
656 were imaged every 10 minutes for 48 h with 30 ms exposures. In order to compensate
657 for focus drift over long-term imaging, a Definite Focus 2 system (Carl Zeiss Microscopy)
658 was employed. Images were captured using an ORCA-Flash 4.0 V2 sCMOS camara with
659 Slidebook 6 microscopy software.
660
661 **Microscopy analysis**
662 All microscopy images were analyzed with ImageJ (National Institutes of Health,
663 Bethesda, MD). Figures for publication were prepared in Adobe Photoshop and Illustrator
664 (Creative Cloud 2022).
665
666 **Statistical analysis**
667 Statistical analysis and graphs were generated using GraphPad Prism 9 software version
668 9.1.1 (GraphPad Software). For morphometric analysis, one-way ANOVA analysis was
669 performed to identify significant differences ($p<0.05$) between cell cycle intermediates for
670 each morphometric measurement. For live-cell analysis, a Power analysis was performed

671 to ensure sufficient n was performed to ensure conclusion was reasonable. For live-cell
672 differential daughter division times, an unpaired two-tailed students t-test was performed
673 to determine if differences observed was statistically significant at the $p<0.05$ significance
674 level. All graphical data was plotted using SuperPlots to show variability among biological
675 replicates [82].
676

677

678 **Figure Legends**

679 **Fig 1. The morphotypes of Trypanosoma cruzi**. All *T. cruzi* morphotypes contain a
680 flagellum that is nucleated from a basal body which is docked to the membrane of the
681 flagellar pocket. The basal body is also connected to the kinetoplast, which is the
682 mitochondrial DNA aggregate. The shape of the cell bodies is defined by a set of
683 subpellicular MTs that underlie the plasma membrane (depicted only in the epimastigote
684 form). In the epimastigote and trypomastigote forms, the flagellum emerges onto the cell
685 surface and is attached to the cell body by the flagellum attachment zone (comprising the
686 MtQ and FAZ filament), both of which extend towards the anterior end of the cell body.
687 The primary morphologic difference between epimastigotes and trypomastigotes is the
688 positioning of the kinetoplast-basal body-flagellar pocket, which is posterior to the nucleus
689 in epimastigotes and anterior in trypomastigotes.

690

691 **Fig 2. *T. cruzi* epimastigotes incorporate tubulin PTMs at the cell posterior during**
692 **cell division.** Epimastigote cells carrying a 3xTy1-mNeonGreen::TcFAZ25 allele were
693 fixed and labeled with 1B41 to label the FAZ and posterior punctum (1B41, magenta),
694 anti-Ty1 to label FAZ25 (TcFAZ25, green), and DAPI to label DNA (DNA, blue). Cells
695 were then imaged using epifluorescence and DIC microscopy. (**A**) Very small 1N1K cells
696 carried a 1B41 punctum at their cell posterior, which was much weaker or absent in larger
697 1N1K cells (**B**). (**C**) The new FAZ was appeared on the dorsal side of the cell and labeled
698 was FAZ25 and 1B41 positive. 1B41 signal appeared at the posterior end at this point.
699 (**D**) As the new FAZ and flagellum extended, the posterior 1B41 punctum increased in

700 brightness. (**E**) Once the cell has begun cytokinesis, the 1B41 punctum is present at the
701 extreme posterior of the cell body. The new-flagellum daughter cell appears to inherit a
702 much shorter new FAZ and flagellum than the old-flagellum daughter. Asterisks highlight
703 the 1B41 posterior punctum labeling, while the arrowheads identify the new FAZ.
704
705 **Fig 3. Defining and quantifying morphogenic intermediates in *T. cruzi* epimastigote**
706 **cell division.** (**A**) Morphogenic intermediates were defined by the presence of a 1B41
707 punctum and if they were the new flagellum or old flagellum daughter (new-flagellum
708 puncta: NF Puncta; old-flagellum puncta: OF puncta), or their nuclear, kinetoplast, and
709 flagellum state (xNxKxF). Note that all cells that have begun to flagellar duplication are
710 labeled with a 1B41 punctum. (**B**) Cell counts over 9 d were used to calculate the cell
711 division time of the Cas9-T7 epimastigote cells line. (**C**) Graph depicting the percentages
712 of cells in each state as defined in (**A**). (**D**) Using the length of the cell cycle as measured
713 in (**B**) and the percentages of cells in different cell cycle states measured in (**C**) allows
714 the calculation of the time that the parasites spend in each state that was defined in (**A**).
715
716 **Fig 4. Quantitation of changes to cell morphology over the course of *T. cruzi***
717 **epimastigote cell division.** (**A**) Cells were fixed and stained with 1B41 to label the FAZ
718 and posterior punctum and DAPI to label DNA. The cells were then imaged using
719 epifluorescence and DIC microscopy, followed by measurement of all the cell features
720 depicted in this schematic. All graphs were generated as SuperPlots, where each
721 independent experiment is shown in a separate color, with the large circles represent the
722 mean of each independent experiment, and black lines represent the mean and the

723 standard deviation. (**B**) Measurements of total cell lengths, which includes flagellar
724 overhang, broken down into the cell division categories defined in **Fig 3A**. (**C**)
725 Measurements of cell body lengths, broken down into the cell division categories defined
726 in **Fig 3A**. (**D**) Measurements of the distance between the cell posterior and the nucleus,
727 broken down into the cell division categories defined in **Fig 3A**. (**E**) Measurements of the
728 distance between the cell posterior to the kinetoplast, broken down into the cell division
729 categories defined in **Fig 3A**. (**F**) Measurements of the length of the old FAZ, broken down
730 into the cell division categories defined in **Fig 3A**. (**G**) Measurements of the length of the
731 old flagellum, broken down into the cell division categories defined in **Fig 3A**. (**H**)
732 Measurements of the width of the cell body, broken down into the cell division categories
733 defined in **Fig 3A**. (**I**) Table showing significance levels between each pair- wise
734 comparison. Statistical analysis was done by one-way ANOVA. ns = not significant, * $p <$
735 0.05, ** $p < 0.01$, ***$p < 0.001$, ****$p < 0.0001$.

736 **Fig 5. The new FAZ does not reach length parity with the old FAZ prior to the**
737 **completion of cell division.** (**A**) Cells were fixed and stained with 1B41 to label the FAZ
738 and posterior punctum and DAPI to label DNA. The cells were then imaged using
739 epifluorescence and DIC microscopy, followed by measurement of all the cell features
740 depicted in this schematic. All graphs were generated as SuperPlots, where each
741 independent experiment is shown in a separate color, with the large circles represent the
742 mean of each independent experiment, and black lines represent the mean and the
743 standard deviation. (**B**) Measurements of the length of the new FAZ as cells progress
744 through cell division. (**C**) Measurements of the length of the new flagellum as cells
745 progress through cell division. (**D**) Ratio of the length of the new FAZ to the old FAZ as

746 cells progress through cell division. (**E**) Ratio of the length of the new flagellum to the old
747 flagellum as cells progress through cell division. Statistical analysis was done by one-way
748 ANOVA ****$p < 0.0001$.

749

750 **Fig 6. TcSAS-6 levels fluctuate on the basal body during cell division.** (**A**) Cells
751 carrying a 3xTy1-mNeonGreen::TcSAS-6 allele were fixed and labeled with 1B41 (1B41,
752 magenta) to label the FAZ and posterior punctum, anti-Ty1 (TcSAS-6, green) to label the
753 basal body, and DAPI to label DNA (DNA, blue). The cells were then imaged using
754 epifluorescence and DIC microscopy. Inserts show a 3X enlargement of the basal body
755 region. The empty arrowheads identify the new flagellum; the asterisks highlight the 1B41
756 posterior punctum. (**B**) Cells carrying a 3xTy1-mNeonGreen::TcSAS-6 allele were fixed
757 and processed for U-ExM. Samples were labeled with anti-Ty1 (TcSAS-6, green) to label
758 the basal body and TAT1 anti-tubulin antibody (Tubulin, magenta) to label the tubulin-
759 containing structures within the cell. The samples were then imaged using SoRa
760 superresolution microscopy. Boxed insets are a 3X magnification of the basal body
761 region. The empty arrowheads identify the mature basal body, while the filled arrowheads
762 identify the probasal body. Scale bars: 10 μm.

763

764 **Fig 7. TcTOEFAZ1 localizes to the ventral side of the flagellum is expressed during**
765 **all cell stages** (**A**) Cells carrying a 3xTy1-mNeonGreen::TcTOEFAZ1 allele were fixed
766 and labeled with 1B41 to label the FAZ and posterior punctum (1B41, magenta), anti-Ty1
767 to label TcTOEFAZ1 (TcTF1, green), and DAPI to label DNA (DNA, blue). The cells were
768 then imaged using fluorescence and DIC microscopy. The asterisks identify the 1B41

769 posterior punctum. (**B**) Cells carrying a 3xTy1-mNeonGreen::TcTOEFAZ1 allele were
770 fixed and processed for U-ExM. Samples were labeled with anti-Ty1 to label TOEFAZ1
771 (TcTF1, green) and TAT1 anti-tubulin antibody to label the tubulin-containing structures
772 within the cell (Tubulin, magenta). The samples were then imaged using SoRa super-
773 resolution microscopy. Boxed insets are a 3X magnification of the basal body region. The
774 empty arrowheads point toward the new flagellum. Scale bars: 10 μm.
775
776 **Fig 8. TcPLK and TcKLIF localize to the FAZ and the posterior punctum during cell**
777 **division.** (**A**) Cells carrying a 3xTy1-mNeonGreen::TcPLK allele were fixed and labeled
778 with 1B41 to label the FAZ and posterior punctum (1B41, magenta), anti-Ty1 to label
779 TcPLK (TcPLK, green), and DAPI to label DNA (DNA, blue). The cells were then imaged
780 using fluorescence and DIC microscopy. Asterisks identify the 1B41 posterior punctum,
781 empty arrowheads show TcPLK recruitment to the cell posterior, and the filled arrowhead
782 shows TcPLK localization to the basal body. (**B**) Cells carrying a 3xTy1-
783 mNeonGreen::TcKLIF allele were fixed and labeled with 1B41 to label the FAZ and
784 posterior punctum (1B41, magenta), anti-Ty1 to label TcKLIF (TcKLIF, green), and DAPI
785 to label DNA (DNA, blue). Asterisks show the 1B41 posterior punctum, empty arrowheads
786 show TcKLIF location to the cell posterior, filled arrowheads show TcKLIF localization to
787 the FAZ, and arrows show TcKLIF localization to the ingressing furrow.
788
789 **Fig 9. *T. cruzi* daughter cells divide at different rates.** (**A**) *T. cruzi* epimastigotes cells
790 were confined in agarose microwells and then imaged using DIC microscopy. Images
791 were taken every 10 min for 2 d. Wells containing one cell were identified and the timing

792 of the first round of division was noted. The time that each daughter cell took to complete
793 a subsequent round of division was recorded. Images show representative still shots of
794 live *T. cruzi* cells undergoing division. In this example, over 220 minutes (3 h, 40 min)
795 elapsed between the division of the first daughter cell and the second. (**B**) Staircase plot
796 showing the timing of the first and second daughter cell divisions. T1/2 for division 1 was
797 12.8 h, while $T_{1/2}$ for division 2 was 17.7 h. (**C**) Plot showing direct comparison of daughter
798 cell division rates. Each line represents daughter cell division times from the same
799 progenitor cell. Cell comparisons are color coded to depict cells imaged in the same live-
800 cell imaging run.
801
802 **Fig 10. Model describing the different stages of epimastigote *T. cruzi* cell division**
803 **described in this work.** (**I**) At the end of cytokinesis, two types of cells are observed:
804 new flagellum daughters (NF Puncta) that are smaller, have a shorter flagellum and FAZ,
805 and a more intense posterior punctum staining with 1B41 and KLF when compared to the
806 old flagellum daughters (OF Puncta). In both cell types the pro and mature basal bodies
807 are labeled with SAS-6 and TOEFAZ1 is present on the dorsal side of the flagellum. **(II)**
808 Once the new flagellum daughter has extended its FAZ and flagellum, the two daughter
809 cells are indistinguishable. The posterior punctum labeling disappears entirely. As the cell
810 begins to divide, PLK is present on the basal body. TOEFAZ1 still labels the dorsal region.
811 **(III)** As the new flagellum is assembled, both PLK and 1B41 labeling become apparent at
812 the cell posterior. PLK is present along the FAZ as well. SAS-6 labeling appears primarily
813 associated with the probasal bodies. The cell begins to widen along its short axis. As the
814 new flagellum and FAZ continue to grow, the KLIF labeling appears at the site where the

815 cleavage furrow will initiate from and is also present at the posterior punctum. TOEFAZ
816 is recruited to cleavage furrow ingression point. Cell widening continues, while the cell
817 posterior shortens along its long axis. **(IV)** As cytokinesis begins, the posterior punctum
818 is labeled with 1B41, PLK, and KLIF and begins to resolve into two discrete structures.
819 KLIF and TOEFAZ are present at the ingressing cleavage furrow, while PLK is present
820 on both FAZ. SAS-6 labeling reappears at the mature basal body.
821
822
823
824

825 **References**

826

827 1. Maslov DA, Votýpka J, Yurchenko V, Lukeš J. Diversity and phylogeny of insect
828 trypanosomatids: all that is hidden shall be revealed. Trends Parasitol. 2012;29: 43 52.
829 doi:10.1016/j.pt.2012.11.001

830 2. d'Avila-Levy CM, Boucinha C, Kostygov A, Santos HLC, Morelli KA, Grybchuk-
831 Ieremenko A, et al. Exploring the environmental diversity of kinetoplastid flagellates in the
832 high-throughput DNA sequencing era. Memórias Instituto Oswaldo Cruz. 2015;110: 956
833 965. doi:10.1590/0074-02760150253

834 3. Lukeš J, Skalický T, Týč J, Votýpka J, Yurchenko V. Evolution of parasitism in
835 kinetoplastid flagellates. Mol Biochem Parasit. 2014;195: 115 122.
836 doi:10.1016/j.molbiopara.2014.05.007

837 4. El-Sayed NM, Myler PJ, Blandin G, Berriman M, Crabtree J, Aggarwal G, et al.
838 Comparative genomics of trypanosomatid parasitic protozoa. Science. 2005;309: 404
839 409. doi:10.1126/science.1112181

840 5. Jackson AP, Allison HC, Barry JD, Field MC, Hertz-Fowler C, Berriman M. A Cell-
841 surface Phylome for African Trypanosomes. Tschudi C, editor. PLoS Neglected Tropical
842 Diseases. 2013;7: e2121. doi:10.1371/journal.pntd.0002121.s003

843 6. Jackson AP, Otto TD, Aslett M, Armstrong SD, Bringaud F, Schlacht A, et al.
844 Kinetoplastid Phylogenomics Reveals the Evolutionary Innovations Associated with the
845 Origins of Parasitism. Curr Biol. 2016;26: 161 172. doi:10.1016/j.cub.2015.11.055

846 7. Wheeler RJ, Gluenz E, Gull K. The Limits on Trypanosomatid Morphological Diversity.
847 Li Z, editor. Plos One. 2013;8: e79581 18. doi:10.1371/journal.pone.0079581

848 8. Wheeler RJ. Use of chiral cell shape to ensure highly directional swimming in
849 trypanosomes. Rao CV, editor. Plos Comput Biol. 2017;13: e1005353 22.
850 doi:10.1371/journal.pcbi.1005353

851 9. Halliday C, Castro-Neto A de, Alcantara CL, Cunha-e-Silva NL, Vaughan S, Sunter JD.
852 Trypanosomatid Flagellar Pocket from Structure to Function. Trends Parasitol. 2020;37:
853 317–329. doi:10.1016/j.pt.2020.11.005

854 10. Wheeler RJ, Gull K, Sunter JD. Coordination of the Cell Cycle in Trypanosomes. Annu
855 Rev Microbiol. 2019;73: 133–154. doi:10.1146/annurev-micro-020518-115617

856 11. Campbell PC, de Graffenried CL. Alternate histories of cytokinesis: lessons from the
857 trypanosomatids. Mol Biol Cell. 2020;31: 2631–2639. doi:10.1091/mbc.e19-12-0696

858 12. Pérez-Molina JA, Molina I. Chagas disease. Lancet. 2018;391: 82–94.
859 doi:10.1016/s0140-6736(17)31612-4

860 13. El-Sayed NM, Myler PJ, Bartholomeu DC, Nilsson D, Aggarwal G, Tran A-N, et al.
861 The genome sequence of Trypanosoma cruzi, etiologic agent of Chagas disease.
862 Science. 2005;309: 409 415. doi:10.1126/science.309.5733.399

863 14. Wang W, Peng D, Baptista RP, Li Y, Kissinger JC, Tarleton RL. Strain-specific
864 genome evolution in Trypanosoma cruzi, the agent of Chagas disease. Plos Pathog.
865 2021;17: e1009254. doi:10.1371/journal.ppat.1009254

866 15. Medeiros LCS, South L, Peng D, Bustamante JM, Wang W, Bunkofske M, et al. Rapid,
867 Selection-Free, High-Efficiency Genome Editing in Protozoan Parasites Using CRISPR-
868 Cas9 Ribonucleoproteins. Boothroyd JC, editor. Mbio. 2017;8: e01788-17 15.
869 doi:10.1128/mbio.01788-17

870 16. Lander N, Li Z-H, Niyogi S, Docampo R. CRISPR/Cas9-Induced Disruption of
871 Paraflagellar Rod Protein 1 and 2 Genes in Trypanosoma cruziReveals Their Role in
872 Flagellar Attachment. Mbio. 2015;6: 495 12. doi:10.1128/mbio.01012-15

873 17. Costa FC, Francisco AF, Jayawardhana S, Calderano SG, Lewis MD, Olmo F, et al.
874 Expanding the toolbox for Trypanosoma cruzi: A parasite line incorporating a
875 bioluminescence-fluorescence dual reporter and streamlined CRISPR/Cas9 functionality
876 for rapid in vivo localisation and phenotyping. Buscaglia CA, editor. Plos Neglect Trop D.
877 2018;12: e0006388 21. doi:10.1371/journal.pntd.0006388

878 18. Simpson AGB, Stevens JR, Lukeš J. The evolution and diversity of kinetoplastid
879 flagellates. Trends Parasitol. 2006;22: 168 174. doi:10.1016/j.pt.2006.02.006

880 19. LukeÅ J, Butenko A, Hashimi H, Maslov DA, Votýpka J, Yurchenko V.
881 Trypanosomatids Are Much More than Just Trypanosomes: Clues from the Expanded
882 Family Tree. Trends Parasitol. 2018;34: 466 480. doi:10.1016/j.pt.2018.03.002

883 20. Field MC, Carrington M. The trypanosome flagellar pocket. Nat Rev Microbiol. 2009;7:
884 775 786. doi:10.1038/nrmicro2221

885 21. Sunter JD, Gull K. The Flagellum Attachment Zone: 'The Cellular Ruler' of
886 Trypanosome Morphology. Trends Parasitol. 2016;32: 309 324.
887 doi:10.1016/j.pt.2015.12.010

888 22. Vickerman K. On the surface coat and flagellar adhesion in trypanosomes. Journal of
889 cell science. 1969;5: 163 193.

890 23. Wheeler RJ, Sunter JD, Gull K. Flagellar pocket restructuring through the Leishmania
891 life cycle involves a discrete flagellum attachment zone. J Cell Sci. 2016;129: 854 867.
892 doi:10.1242/jcs.183152

24. Alcantara CL, Souza W, Silva NLC e. The cytostome-cytopharynx complex of intracellular and extracellular amastigotes of Trypanosoma cruzi exhibit structural and functional differences. Cell Microbiol. 2021;23: e13346. doi:10.1111/cmi.13346

25. Alcantara C de L, Vidal JC, Souza W de, Cunha-e-Silva NL. The cytostome–cytopharynx complex of Trypanosoma cruzi epimastigotes disassembles during cell division. J Cell Sci. 2017;130: 164–176. doi:10.1242/jcs.187419

26. Sinclair AN, de Graffenried CL. More than Microtubules: The Structure and Function of the Subpellicular Array in Trypanosomatids. Trends Parasitol. 2019;35: 760–777. doi:10.1016/j.pt.2019.07.008

27. Souto-Padrón T, Souza W de, Heuser JE. Quick-freeze, deep-etch rotary replication of Trypanosoma cruzi and Herpetomonas megaseliae. J Cell Sci. 1984;69: 167–78.

28. Engstler M, Pfohl T, Herminghaus S, Boshart M, Wiegertjes G, Heddergott N, et al. Hydrodynamic flow-mediated protein sorting on the cell surface of trypanosomes. Cell. 2007;131: 505 515. doi:10.1016/j.cell.2007.08.046

29. Heddergott N, Krüger T, Babu SB, Wei A, Stellamanns E, Uppaluri S, et al. Trypanosome Motion Represents an Adaptation to the Crowded Environment of the Vertebrate Bloodstream. Beverley SM, editor. PLoS pathogens. 2012;8: e1003023. doi:10.1371/journal.ppat.1003023.t002

30. Sunter J, Gull K. Shape, form, function and Leishmania pathogenicity: from textbook descriptions to biological understanding. Royal Soc Open Biology. 2017;7: 170165. doi:10.1098/rsob.170165

31. Sharma R, Peacock L, Gluenz E, Gull K, Gibson W, Carrington M. Asymmetric cell division as a route to reduction in cell length and change in cell morphology in trypanosomes. Protist. 2008;159: 137 151. doi:10.1016/j.protis.2007.07.004

32. Hyde TP, Dvorak JA. Trypanosoma cruzi: Interaction with vertebrate cells in vitro II. Quantitative analysis of the penetration phase. Exp Parasitol. 1973;34: 284–294. doi:10.1016/0014-4894(73)90088-x

33. Rotureau B, Subota I, Buisson J, Bastin P. A new asymmetric division contributes to the continuous production of infective trypanosomes in the tsetse fly. Development. 2012;139: 1842 1850. doi:10.1242/dev.072611

34. Lacomble S, Vaughan S, Gadelha C, Morphew MK, Shaw MK, McIntosh JR, et al. Three-dimensional cellular architecture of the flagellar pocket and associated cytoskeleton in trypanosomes revealed by electron microscope tomography. J Cell Sci. 2009;122: 1081 1090. doi:10.1242/jcs.045740

927 35. Sherwin T, Gull K. Visualization of detyrosination along single microtubules reveals
928 novel mechanisms of assembly during cytoskeletal duplication in trypanosomes. Cell.
929 1989;57: 211 221. doi:10.1016/0092-8674(89)90959-8

930 36. Wheeler RJ, Scheumann N, Wickstead B, Gull K, Vaughan S. Cytokinesis in
931 Trypanosoma brucei differs between bloodstream and tsetse trypomastigote forms:
932 implications for microtubule-based morphogenesis and mutant analysis. Mol Microbiol.
933 2013;90: 1339 1355. doi:10.1111/mmi.12436

934 37. Wheeler RJ, Gluenz E, Gull K. The cell cycle of Leishmania: morphogenetic events
935 and their implications for parasite biology. Mol Microbiol. 2011;79: 647 662.
936 doi:10.1111/j.1365-2958.2010.07479.x

937 38. Shaner NC, Lambert GG, Chammas A, Ni Y, Cranfill PJ, Baird MA, et al. A bright
938 monomeric green fluorescent protein derived from Branchiostoma lanceolatum. Nat
939 Methods. 2013;10: 407 409. doi:10.1038/nmeth.2413

940 39. Bastin P, Bagherzadeh Z, Matthews KR, Gull K. A novel epitope tag system to study
941 protein targeting and organelle biogenesis in Trypanosoma brucei. Mol Biochem Parasit.
942 1996;77: 235 239. doi:10.1016/0166-6851(96)02598-4

943 40. Amos B, Aurrecoechea C, Barba M, Barreto A, Basenko EY, Bażant W, et al.
944 VEuPathDB: the eukaryotic pathogen, vector and host bioinformatics resource center.
945 Nucleic Acids Res. 2021;50: D898–D911. doi:10.1093/nar/gkab929

946 41. Halliday C, Billington K, Wang Z, Madden R, Dean S, Sunter JD, et al. Cellular
947 landmarks of Trypanosoma brucei and Leishmania mexicana. Mol Biochem Parasit.
948 2019;230: 24 36. doi:10.1016/j.molbiopara.2018.12.003

949 42. Billington K, Halliday C, Madden R, Dyer P, Barker AR, Moreira-Leite FF, et al.
950 Genome-wide subcellular protein map for the flagellate parasite Trypanosoma brucei. Nat
951 Microbiol. 2023;8: 533–547. doi:10.1038/s41564-022-01295-6

952 43. Gallo JM, Précigout E, Schrével J. Subcellular sequestration of an antigenically
953 unique beta-tubulin. Cell Motil Cytoskel. 1988;9: 175 183. doi:10.1002/cm.970090209

954 44. Gallo JM, Précigout E. Tubulin expression in trypanosomes. Biology of the cell / under
955 the auspices of the European Cell Biology Organization. 1988;64: 137 143.

956 45. Rocha GM, Brandão BA, Mortara RA, Attias M, Souza W de, Carvalho TMU. The
957 flagellar attachment zone of Trypanosoma cruzi epimastigote forms. J Struct Biol.
958 2006;154: 89 99. doi:10.1016/j.jsb.2005.11.008

959 46. Abeywickrema M, Vachova H, Farr H, Mohr T, Wheeler RJ, Lai D, et al. Non-
960 equivalence in old- and new-flagellum daughter cells of a proliferative division in
961 Trypanosoma brucei. Mol Microbiol. 2019. doi:10.1111/mmi.14345

962 47. Wehland J. A rat monoclonal antibody reacting specifically with the tyrosylated form
963 of alpha-tubulin. I. Biochemical characterization, effects on microtubule polymerization in
964 vitro, and microtubule polymerization and organization in vivo. J Cell Biology. 1983;97:
965 1467 1475. doi:10.1083/jcb.97.5.1467

966 48. Wehland J. A rat monoclonal antibody reacting specifically with the tyrosylated form
967 of alpha-tubulin. II. Effects on cell movement, organization of microtubules, and
968 intermediate filaments, and arrangement of Golgi elements. J Cell Biology. 1983;97: 1476
969 1490. doi:10.1083/jcb.97.5.1476

970 49. Sasse R, Gull K. Tubulin post-translational modifications and the construction of
971 microtubular organelles in Trypanosoma brucei. Journal of cell science. 1988;90 (Pt 4):
972 577 589.

973 50. Wolff A, Néchaud B de, Chillet D, Mazarguil H, Desbruyères E, Audebert S, et al.
974 Distribution of glutamylated alpha and beta-tubulin in mouse tissues using a specific
975 monoclonal antibody, GT335. Eur J Cell Biol. 1992;59: 425–32.

976 51. Casanova M, Monbrison F de, Dijk J van, Janke C, Pagès M, Bastien P.
977 Characterisation of polyglutamylases in trypanosomatids. Int J Parasitol. 2015;45: 121
978 132. doi:10.1016/j.ijpara.2014.09.005

979 52. Piperno G, Fuller MT. Monoclonal antibodies specific for an acetylated form of alpha-
980 tubulin recognize the antigen in cilia and flagella from a variety of organisms. J Cell
981 Biology. 1985;101: 2085–2094. doi:10.1083/jcb.101.6.2085

982 53. Sherwin T, Gull K. The cell division cycle of Trypanosoma brucei brucei: timing of
983 event markers and cytoskeletal modulations. Philosophical Transactions Royal Soc Lond
984 Ser B Biological Sci. 1989;323: 573 588. doi:10.1098/rstb.1989.0037

985 54. CONTOIS DE. Kinetics of bacterial growth: relationship between population density
986 and specific growth rate of continuous cultures. Journal of general microbiology. 1959;21:
987 40 50.

988 55. Leidel S, Delattre M, Cerutti L, Baumer K, Gönczy P. SAS-6 defines a protein family
989 required for centrosome duplication in C. elegans and in human cells. Nat Cell Biol.
990 2005;7: 115–125. doi:10.1038/ncb1220

991 56. Hu H, Liu Y, Zhou Q, Siegel S, Li Z. The Centriole Cartwheel Protein SAS-6 in
992 Trypanosoma brucei Is Required for Probasal Body Biogenesis and Flagellum Assembly.
993 Eukaryot Cell. 2015;14: 898–907. doi:10.1128/ec.00083-15

994 57. He CY, Pypaert M, Warren G. Golgi duplication in Trypanosoma brucei requires
995 Centrin2. Science. 2005;310: 1196 1198. doi:10.1126/science.1119969

996 58. Gambarotto D, Zwettler FU, Guennec ML, Schmidt-Cernohorska M, Fortun D,
997 Borgers S, et al. Imaging cellular ultrastructures using expansion microscopy (U-ExM).
998 Nat Methods. 2019;16: 71–74. doi:10.1038/s41592-018-0238-1

999 59. Kalichava A, Ochsenreiter T. Ultrastructure expansion microscopy in Trypanosoma
1000 brucei. Open Biol. 2021;11: 210132. doi:10.1098/rsob.210132

1001 60. Gorilak P, Pružincová M, Vachova H, Olšinová M, Cernohorska MS, Varga V.
1002 Expansion microscopy facilitates quantitative super-resolution studies of cytoskeletal
1003 structures in kinetoplastid parasites. Open Biol. 2021;11: 210131.
1004 doi:10.1098/rsob.210131

1005 61. Azuma T, Kei T. Super-resolution spinning-disk confocal microscopy using optical
1006 photon reassignment. Opt Express. 2015;23: 15003–15011. doi:10.1364/oe.23.015003

1007 62. Woods A, Sherwin T, Sasse R, MacRae TH, Baines AJ, Gull K. Definition of individual
1008 components within the cytoskeleton of Trypanosoma brucei by a library of monoclonal
1009 antibodies. Journal of cell science. 1989;93 (Pt 3): 491 500.

1010 63. McAllaster MR, Ikeda KN, Lozano-Núñez A, Anrather D, Unterwurzacher V,
1011 Gossenreiter T, et al. Proteomic identification of novel cytoskeletal proteins associated
1012 with TbPLK, an essential regulator of cell morphogenesis in Trypanosoma brucei. Mol
1013 Biol Cell. 2015;26: 3013 3029. doi:10.1091/mbc.e15-04-0219

1014 64. Zhou Q, Gu J, Lun Z-R, Ayala FJ, Li Z. Two distinct cytokinesis pathways drive
1015 trypanosome cell division initiation from opposite cell ends. Proc National Acad Sci.
1016 2016;113: 3287 3292. doi:10.1073/pnas.1601596113

1017 65. Sinclair-Davis AN, McAllaster MR, de Graffenried CL. A functional analysis of
1018 TOEFAZ1 uncovers protein domains essential for cytokinesis in Trypanosoma brucei. J
1019 Cell Sci. 2017;130: 3918 3932. doi:10.1242/jcs.207209

1020 66. Zhou Q, Hu H, Li Z. An EF-hand-containing Protein in Trypanosoma brucei Regulates
1021 Cytokinesis Initiation by Maintaining the Stability of the Cytokinesis Initiation Factor CIF1.
1022 J Biol Chem. 2016;291: 14395 14409. doi:10.1074/jbc.m116.726133

1023 67. Kurasawa Y, An T, Li Z. Polo-like kinase in trypanosomes: an odd member out of the
1024 Polo family. Open Biol. 2020;10: 200189. doi:10.1098/rsob.200189

1025 68. Ikeda KN, de Graffenried CL. Polo-like kinase is necessary for flagellum inheritance
1026 in Trypanosoma brucei. J Cell Sci. 2012;125: 3173 3184. doi:10.1242/jcs.101162

1027 69. Zhou Q, Hu H, Li Z. KLIF-associated cytoskeletal proteins in Trypanosoma brucei
1028 regulate cytokinesis by promoting cleavage furrow positioning and ingression. J Biological
1029 Chem. 2022;298: 101943. doi:10.1016/j.jbc.2022.101943

1030 70. Hilton NA, Sladewski TE, Perry JA, Pataki Z, Sinclair-Davis AN, Muniz RS, et al.
1031 Identification of TOEFAZ1-interacting proteins reveals key regulators of Trypanosoma
1032 brucei cytokinesis. Mol Microbiol. 2018;109: 306 326. doi:10.1111/mmi.13986

1033 71. Sladewski TE, Campbell PC, Billington N, D'Ordine A, Cole JL, de Graffenried CL.
1034 Cytokinesis in Trypanosoma brucei relies on an orphan kinesin that dynamically
1035 crosslinks microtubules. Curr Biol. 2023;33: 899-911.e5. doi:10.1016/j.cub.2023.01.035

1036 72. Muniz RS, Campbell PC, Sladewski TE, Renner LD, de Graffenried CL. Revealing
1037 spatio-temporal dynamics with long-term trypanosomatid live-cell imaging. Plos Pathog.
1038 2022;18: e1010218. doi:10.1371/journal.ppat.1010218

1039 73. Saraiva FMS, Cosentino-Gomes D, Inacio JDF, Almeida-Amaral EE, Louzada-Neto
1040 O, Rossini A, et al. Hypoxia Effects on Trypanosoma cruzi Epimastigotes Proliferation,
1041 Differentiation, and Energy Metabolism. Pathogens. 2022;11: 897.
1042 doi:10.3390/pathogens11080897

1043 74. Elias MC, Cunha JPC da, Faria FP de, Mortara RA, Freymüller E, Schenkman S.
1044 Morphological events during the Trypanosoma cruzi cell cycle. Protist. 2007;158: 147
1045 157. doi:10.1016/j.protis.2006.10.002

1046 75. Kohl L, Sherwin T, Gull K. Assembly of the paraflagellar rod and the flagellum
1047 attachment zone complex during the Trypanosoma brucei cell cycle. J Eukaryot Microbiol.
1048 1999;46: 105 109. doi:10.1111/j.1550-7408.1999.tb04592.x

1049 76. Kitagawa D, Vakonakis I, Olieric N, Hilbert M, Keller D, Olieric V, et al. Structural Basis
1050 of the 9-Fold Symmetry of Centrioles. Cell. 2011;144: 364–375.
1051 doi:10.1016/j.cell.2011.01.008

1052 77. Breugel M van, Hirono M, Andreeva A, Yanagisawa H, Yamaguchi S, Nakazawa Y,
1053 et al. Structures of SAS-6 Suggest Its Organization in Centrioles. Science. 2011;331:
1054 1196–1199. doi:10.1126/science.1199325

1055 78. Fong CS, Kim M, Yang TT, Liao J-C, Tsou M-FB. SAS-6 Assembly Templated by the
1056 Lumen of Cartwheel-less Centrioles Precedes Centriole Duplication. Dev Cell. 2014;30:
1057 238–245. doi:10.1016/j.devcel.2014.05.008

1058 79. Scheumann N. Functions of conserved centriole proteins in African trypanosomes.
1059 University of Oxford. 2012.

1060 80. Skalický T, Dobáková E, Wheeler RJ, Tesařová M, Flegontov P, Jirsová D, et al.
1061 Extensive flagellar remodeling during the complex life cycle of Paratrypanosoma, an
1062 early-branching trypanosomatid. Proc National Acad Sci. 2017;114: 11757 11762.
1063 doi:10.1073/pnas.1712311114

1064 81. Beneke T, Madden R, Makin L, Valli J, Sunter J, Gluenz E. A CRISPR Cas9 high-
1065 throughput genome editing toolkit for kinetoplastids. Roy Soc Open Sci. 2017;4: 170095
1066 16. doi:10.1098/rsos.170095

1067 82. Lord SJ, Velle KB, Mullins RD, Fritz-Laylin LK. SuperPlots: Communicating
1068 reproducibility and variability in cell biology. J Cell Biol. 2020;219: e202001064.
1069 doi:10.1083/jcb.202001064

1070

1071

1072 **Supplemental Figure legends**

1073 **S1 Fig. Antibodies against established tubulin post-translational modifications do**
1074 **not label the 1B41-positive posterior punctum**. *T. cruzi* cells were fixed, then labeled
1075 with anti-tyrosinated tubulin (YL1/2), polyglutamylated tubulin (GT335 or IN105), or
1076 acetylated tubulin (6-11 B-1), followed by secondary antibodies conjugated to Alexa488,
1077 and DAPI to label DNA. Cells were then imaged using epifluorescence and DIC
1078 microscopy.

1079

1080 **S2 Fig. The parental *T. cruzi* Y strain cell line and the *T. cruzi* Brazil A4 strain both**
1081 **show asymmetric cell division and a 1B41-positive punctum at the cell posterior.**
1082 (**A**) The parental *T. cruzi* Y strain used for making all the tagged cell lines in this work was
1083 fixed and then labeled with 1B41 antibody, followed by fluorescently conjugated
1084 secondary antibodies and DAPI to label the DNA. The cells were imaged using
1085 immunofluorescence and DIC microscopy. Asterisks highlight the 1B41 posterior
1086 punctum labeling, while the arrowheads identify the new FAZ. (**B**) Measurements of the
1087 total cell length as defined in Fig 4A. (**C**) Measurements of the cell body length as defined
1088 in Fig 4A (**D**) Measurements of the Old FAZ length as defined in Fig 4A (**E**) Measurements
1089 of the posterior to nucleus distance as defined in Fig 4A. (**F**) Measurements of the
1090 posterior to kinetoplast distance as defined in Fig 4A (**G**) Measurements of the cell body
1091 with as defined in Fig 4A. (**H**) *T. cruzi* Brazil A4 strain cells were fixed and labeled with
1092 1B41, followed by fluorescently conjugated secondary antibodies and DAPI to label the
1093 DNA. The cells were then imaged using immunofluorescence microscopy.

1094

1095 **S3 Fig. TcSAS-6 does not persistently label the pro- and mature-basal body in *T.***
1096 ***cruzi* epimastiogtes.** (**A**) Cells carrying a 3xTy1-mNeonGreen::TcSAS-6 allele were
1097 fixed and labeled with anti-Ty1 and 20H5 to label SAS-6 and TcCentrin2, followed by
1098 fluorescently labelled secondary antibodies and DAPI to label DNA. The cells were then
1099 imaged using immunofluorescence microscopy. Insets show a 3X magnification of the
1100 basal body regions. (**B**) Cells carrying a 3xTy1-mNeonGreen::TcSAS-6 allele were fixed
1101 and then incubated with DAPI to label the DNA. The innate mNeonGreen fluorescence
1102 was then imaged using epifluorescence microscopy.
1103
1104 **S4 Fig. Western blotting validation of the tagged cell lines used in this work.** The
1105 KLIF, PLK, FAZ25, TOEFAZ1, and SAS-6 cell lines endogenously tagged with 3X Ty1-
1106 mNeonGreen were harvested and then lysed in SDS-PAGE loading buffer, followed by
1107 fractionation using SDS-PAGE. Fractionated lysates were transferred to nitrocellulose
1108 and probed with anti-Ty1 antibody.
1109
1110 **S1 Movie. *T. cruzi* epimastigote cell division produces daughter cells with very**
1111 **different rates of subsequent division events.** *T. cruzi* Y strain cells expressing Cas9
1112 and T7 polymerase were plated in 50x50x6 μm agarose microwells and imaged with a
1113 20×/0.8 NA lens. DIC images were captured every 10 min for 48 h. Video depicts images
1114 portrayed in Fig 9A.
1115
1116 **S1. Table. All the primers that were used to generate gDNAs and the healing**
1117 **constructs for gene tagging.**

1118

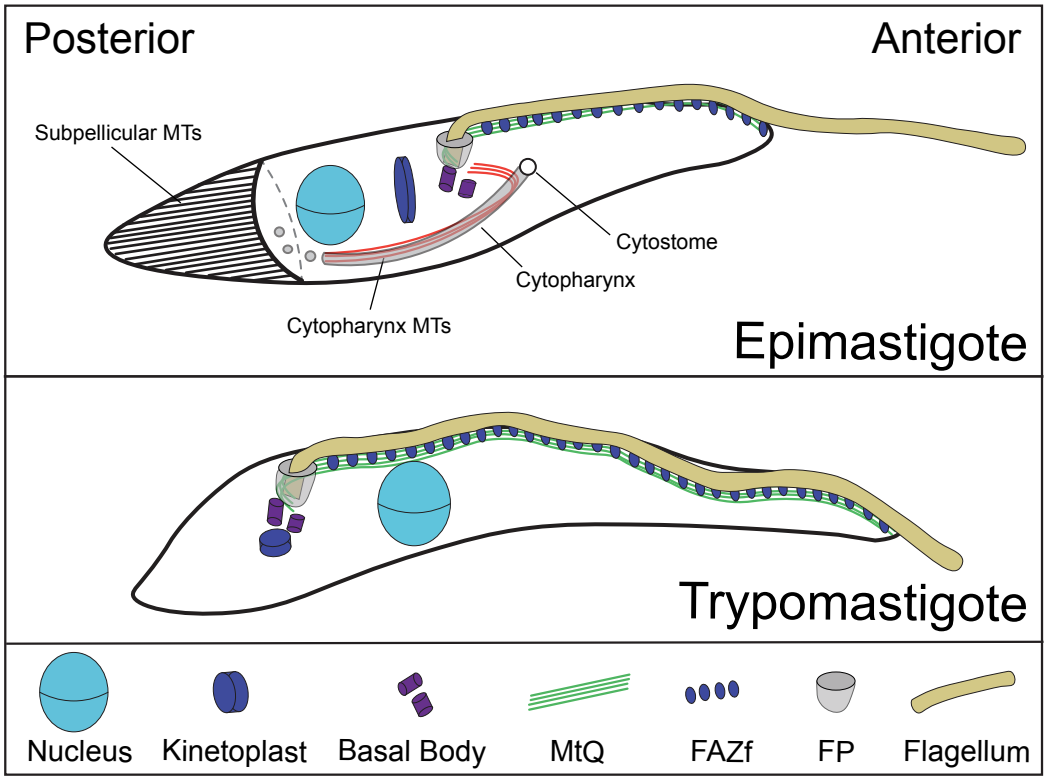
Posterior
Anterior
Subpellicular MTs
Cytostome
Cytopharynx
Cytopharynx MTs
Epimastigote
Trypomastigote
Nucleus
Kinetoplast
Basal Body
MtQ
FAZf
FP
Flagellum

Fig 1

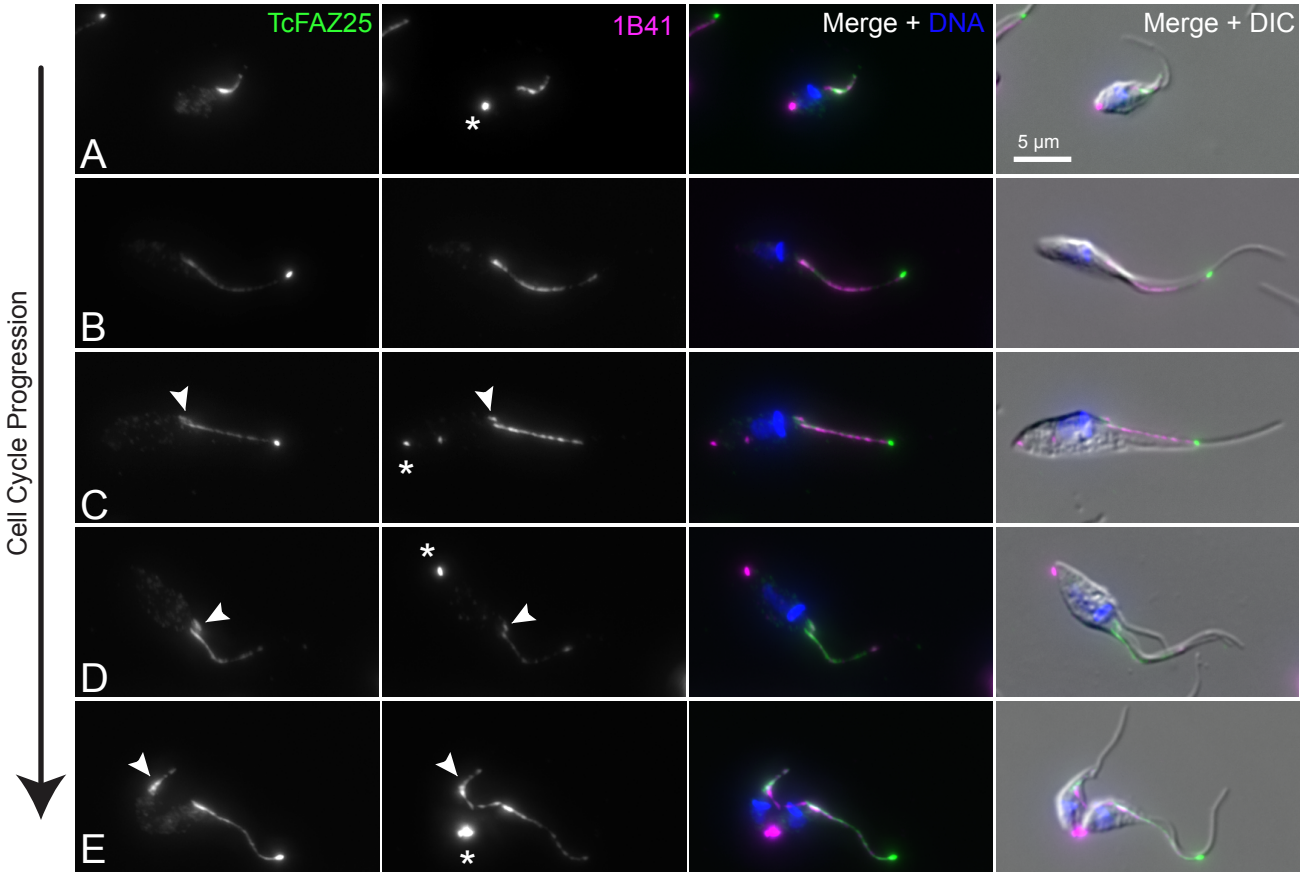
TcFAZ25
1B41
Merge + DNA
Merge + DIC
5 µm
Cell Cycle Progression
A
B
C
D
E

Fig 2

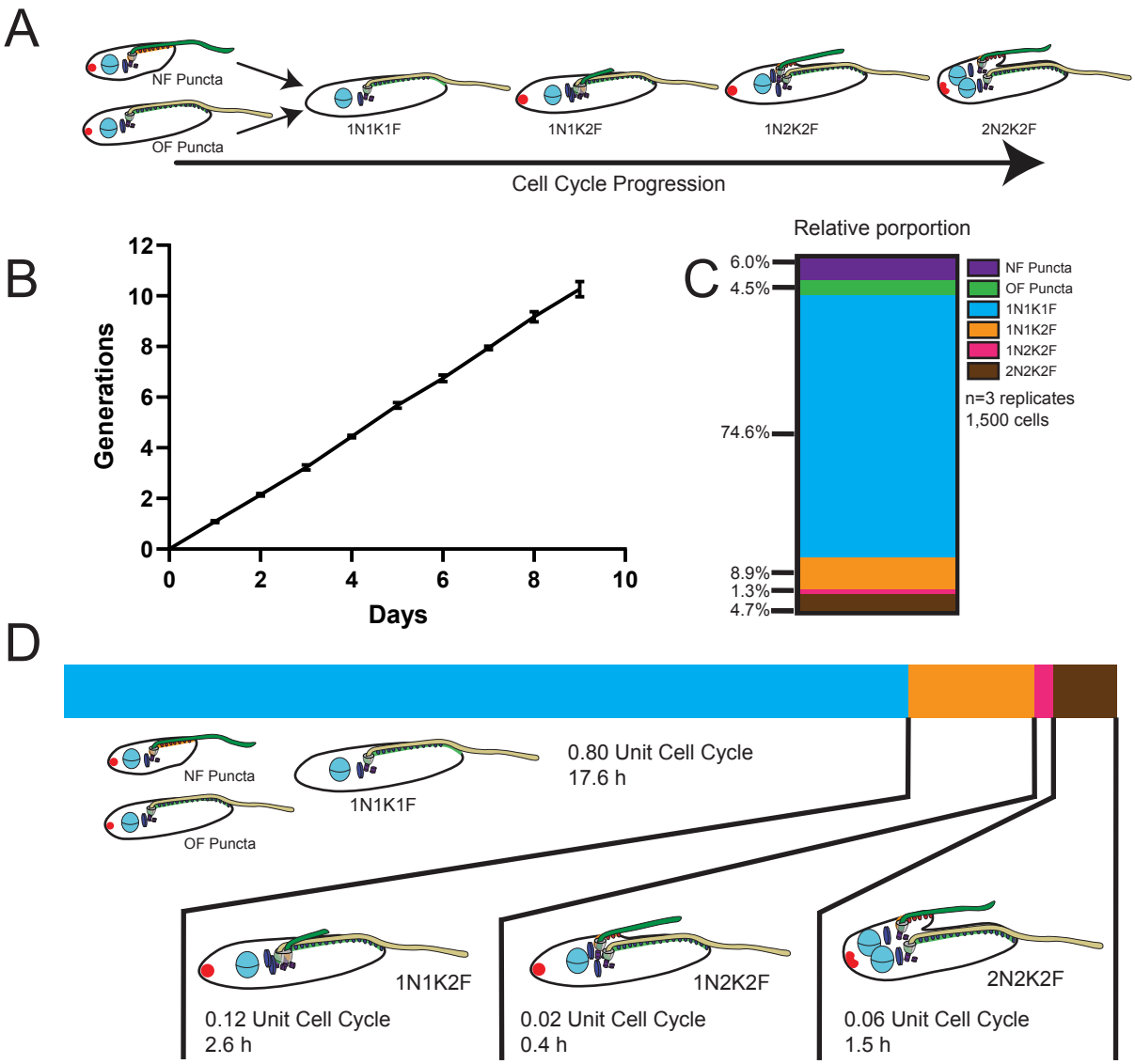
A
NF Puncta
OF Puncta
1N1K1F
1N1K2F
1N2K2F
2N2K2F
Cell Cycle Progression
B
Generations
Days
0
2
4
6
8
10
12
C
Relative porportion
6.0%
4.5%
74.6%
8.9%
1.3%
4.7%
NF Puncta
OF Puncta
1N1K1F
1N1K2F
1N2K2F
2N2K2F
n=3 replicates
1,500 cells
D
NF Puncta
OF Puncta
1N1K1F
0.80 Unit Cell Cycle
17.6 h
1N1K2F
0.12 Unit Cell Cycle
2.6 h
1N2K2F
0.02 Unit Cell Cycle
0.4 h
2N2K2F
0.06 Unit Cell Cycle
1.5 h

Fig 3

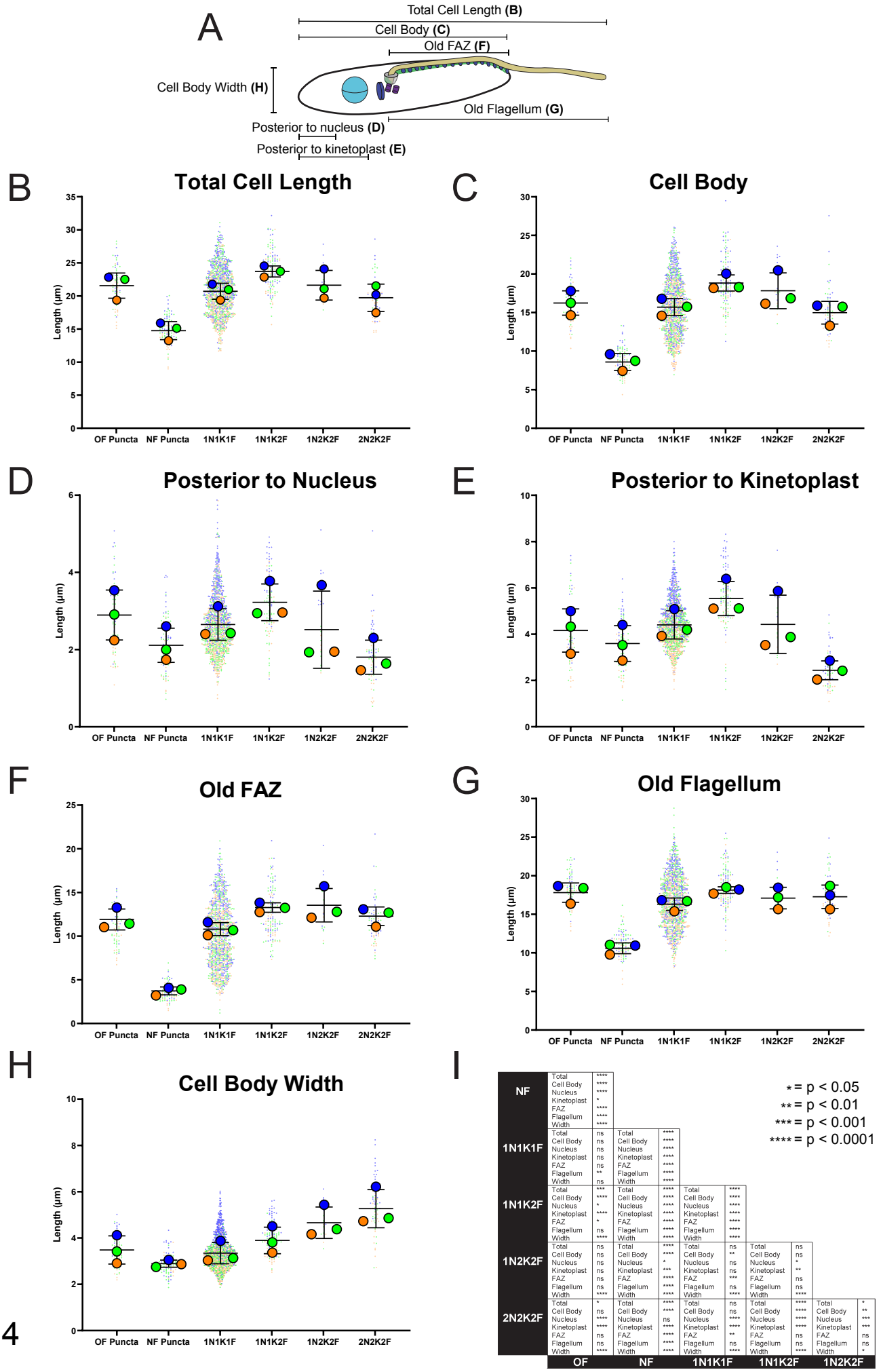
A
Total Cell Length (B)
Cell Body (C)
Old FAZ (F)
Cell Body Width (H)
Old Flagellum (G)
Posterior to nucleus (D)
Posterior to kinetoplast (E)
B
Total Cell Length
C
Cell Body
D
Posterior to Nucleus
E
Posterior to Kinetoplast
F
Old FAZ
G
Old Flagellum
H
Cell Body Width
Length (µm)
OF Puncta
NF Puncta
1N1K1F
1N1K2F
1N2K2F
2N2K2F
I
* = p < 0.05
** = p < 0.01
*** = p < 0.001
**** = p < 0.0001
NF
1N1K1F
1N1K2F
1N2K2F
2N2K2F
OF
NF
1N1K1F
1N1K2F
1N2K2F

Fig 4

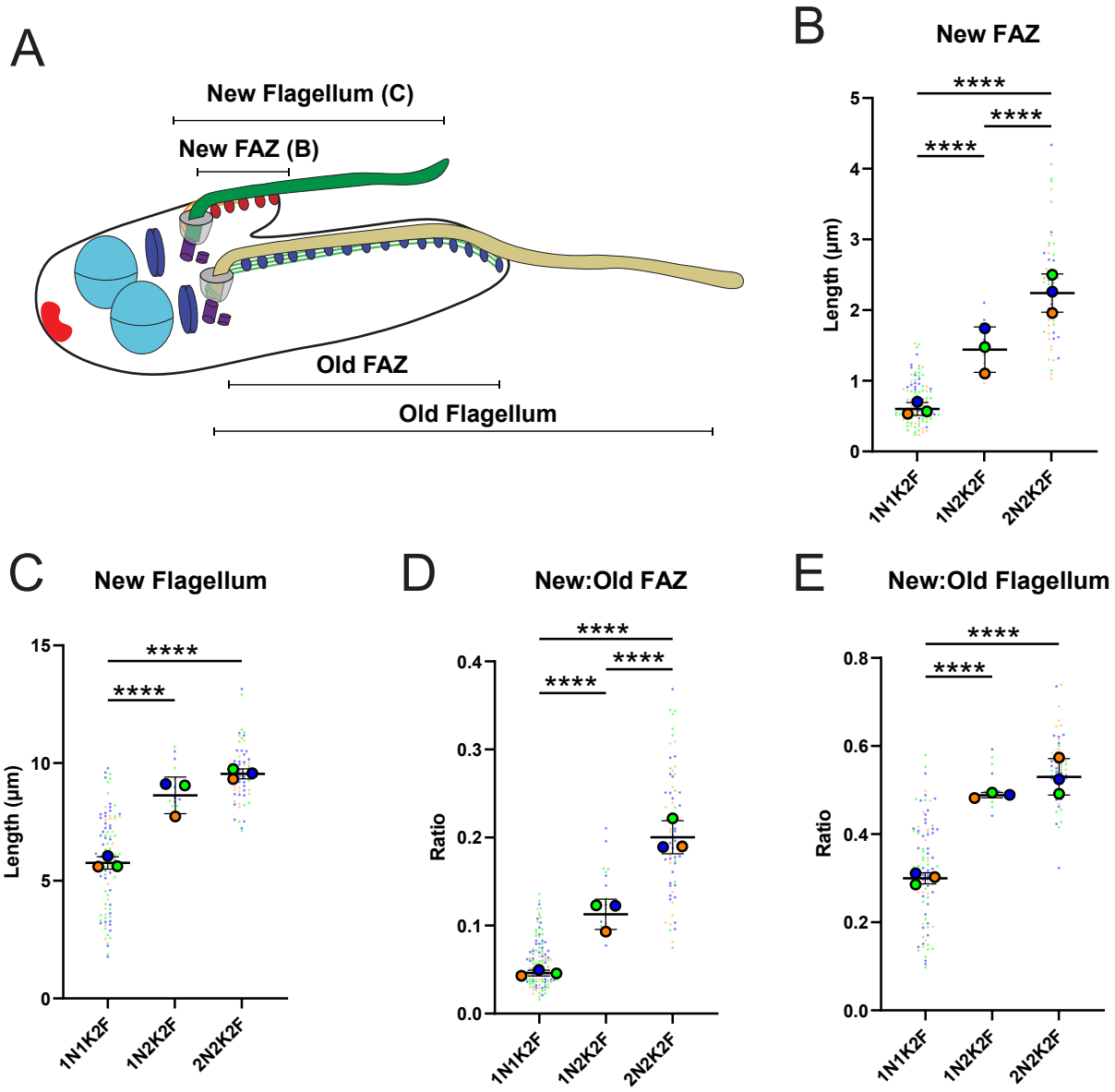
A
New Flagellum (C)
New FAZ (B)
Old FAZ
Old Flagellum
B
New FAZ
Length (µm)
****
****
****
1N1K2F
1N2K2F
2N2K2F
C
New Flagellum
Length (µm)
****
****
D
New:Old FAZ
Ratio
E
New:Old Flagellum
Ratio

Fig 5

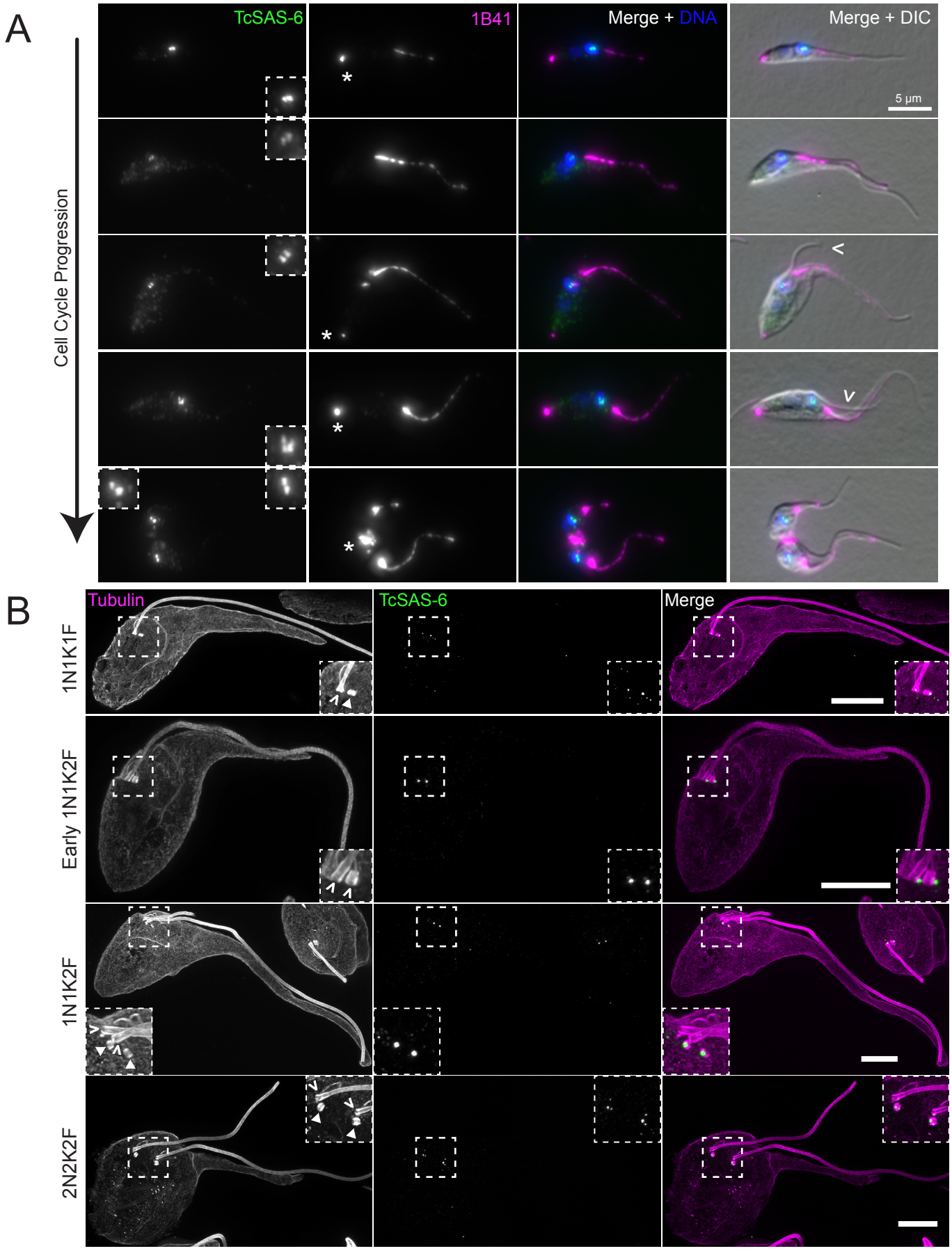
A
TcSAS-6
1B41
Merge + DNA
Merge + DIC
5 µm
Cell Cycle Progression
B
Tubulin
TcSAS-6
Merge
1N1K1F
Early 1N1K2F
1N1K2F
2N2K2F

Fig 6

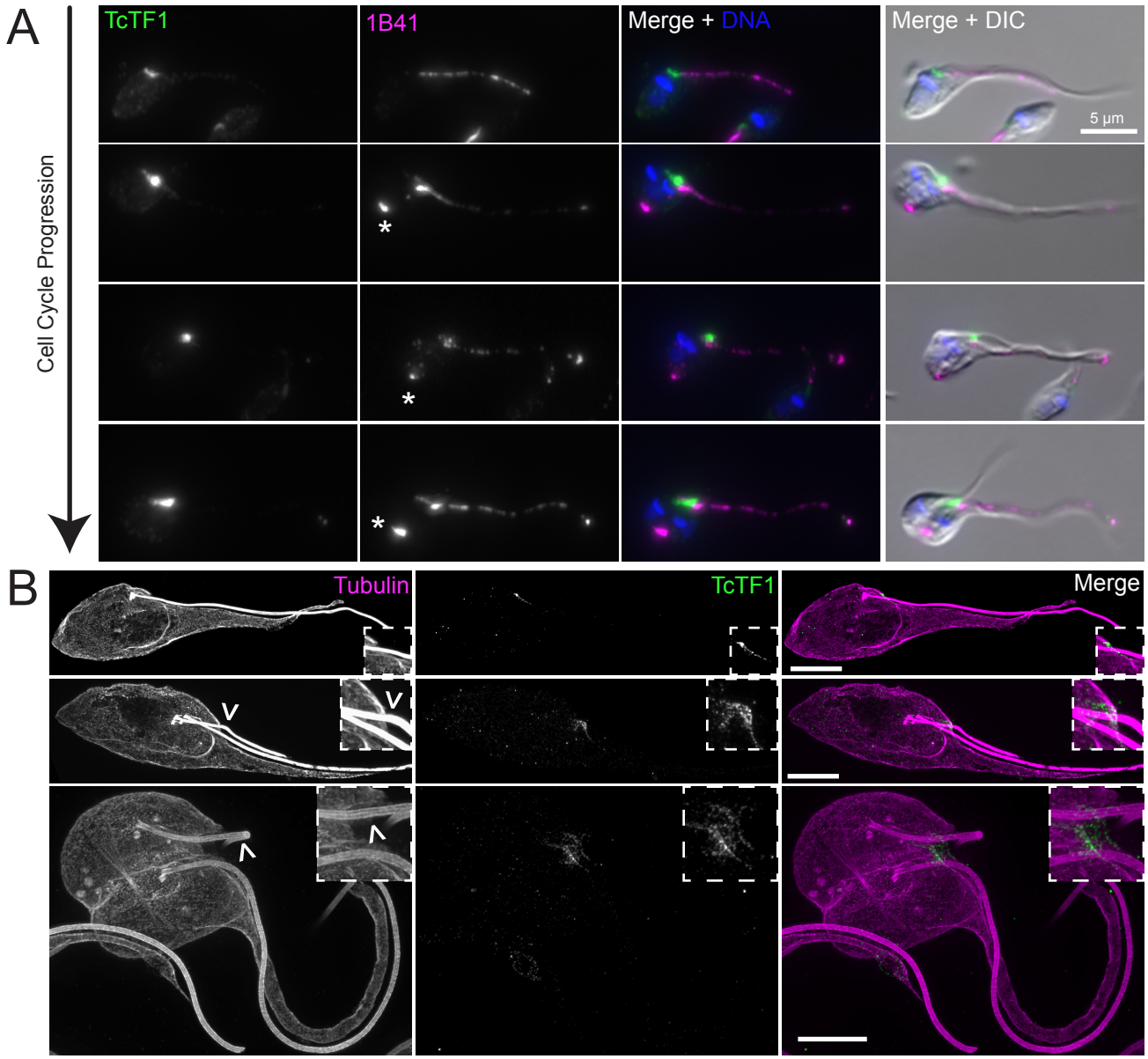
A
TcTF1
1B41
Merge + DNA
Merge + DIC
5 µm
Cell Cycle Progression
B
Tubulin
TcTF1
Merge

Fig 7

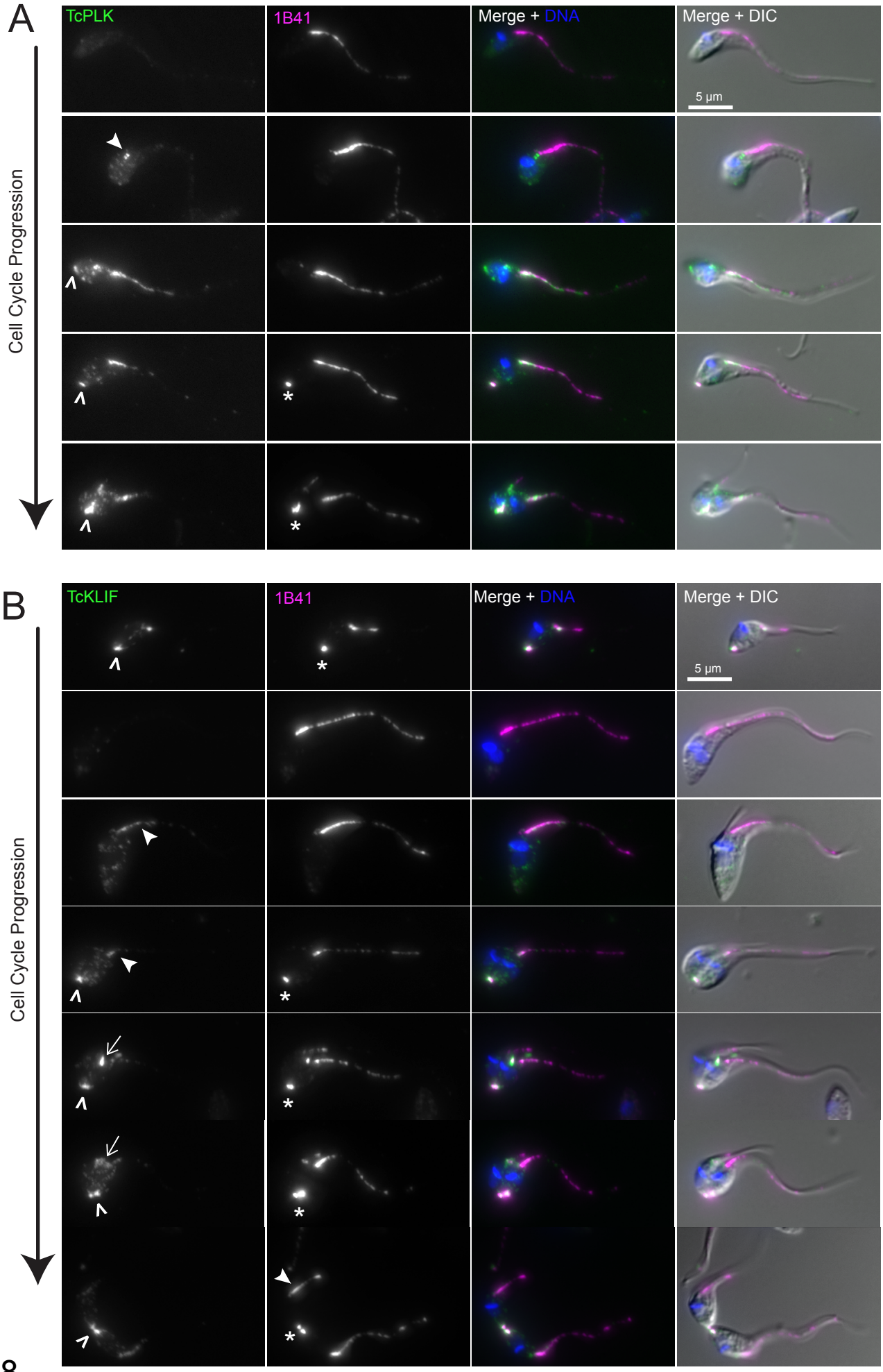
A
TcPLK
1B41
Merge + DNA
Merge + DIC
5 µm
Cell Cycle Progression
B
TcKLIF
1B41
Merge + DNA
Merge + DIC
5 µm
Cell Cycle Progression

Fig 8

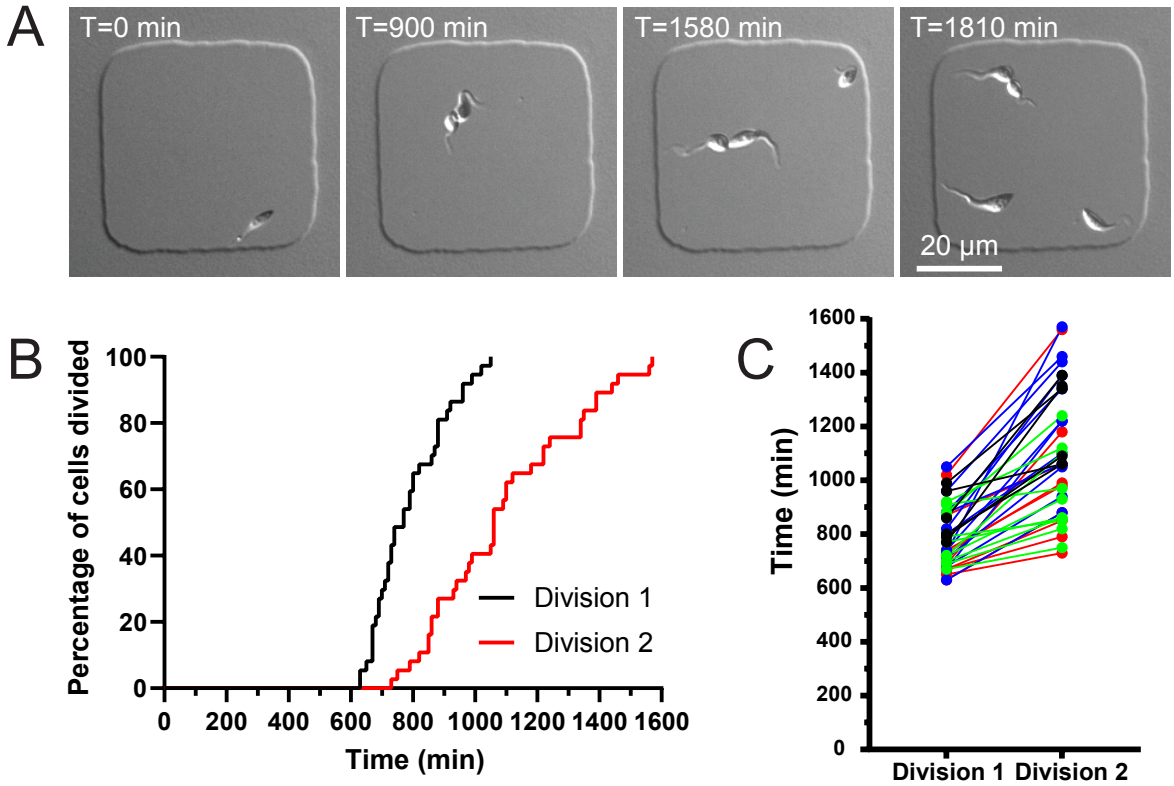
A
T=0 min
T=900 min
T=1580 min
T=1810 min
20 µm
B
Percentage of cells divided
100
80
60
40
20
0
0
200
400
600
800
1000
1200
1400
1600
Time (min)
Division 1
Division 2
C
Time (min)
1600
1400
1200
1000
800
600
400
200
0
Division 1
Division 2

Fig 9

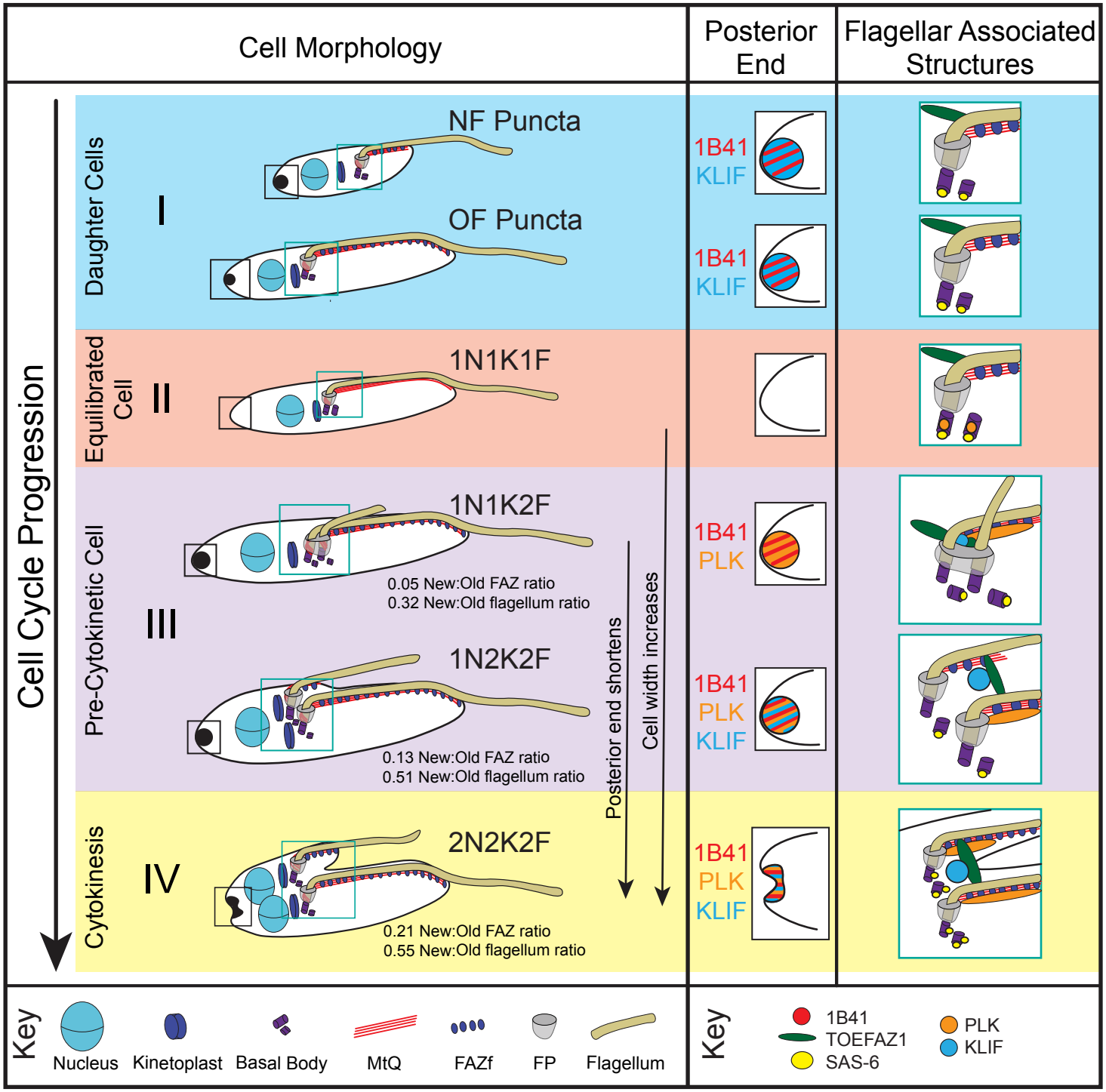
Cell Morphology
Posterior End
Flagellar Associated Structures
Cell Cycle Progression
Daughter Cells
I
NF Puncta
OF Puncta
1B41
KLIF
1B41
KLIF
Equilibrated Cell
II
1N1K1F
Pre-Cytokinetic Cell
III
1N1K2F
0.05 New:Old FAZ ratio
0.32 New:Old flagellum ratio
1B41
PLK
1N2K2F
0.13 New:Old FAZ ratio
0.51 New:Old flagellum ratio
1B41
PLK
KLIF
Posterior end shortens
Cell width increases
Cytokinesis
IV
2N2K2F
0.21 New:Old FAZ ratio
0.55 New:Old flagellum ratio
1B41
PLK
KLIF
Key
Nucleus
Kinetoplast
Basal Body
MtQ
FAZf
FP
Flagellum
Key
1B41
TOEFAZ1
SAS-6
PLK
KLIF

Fig 10

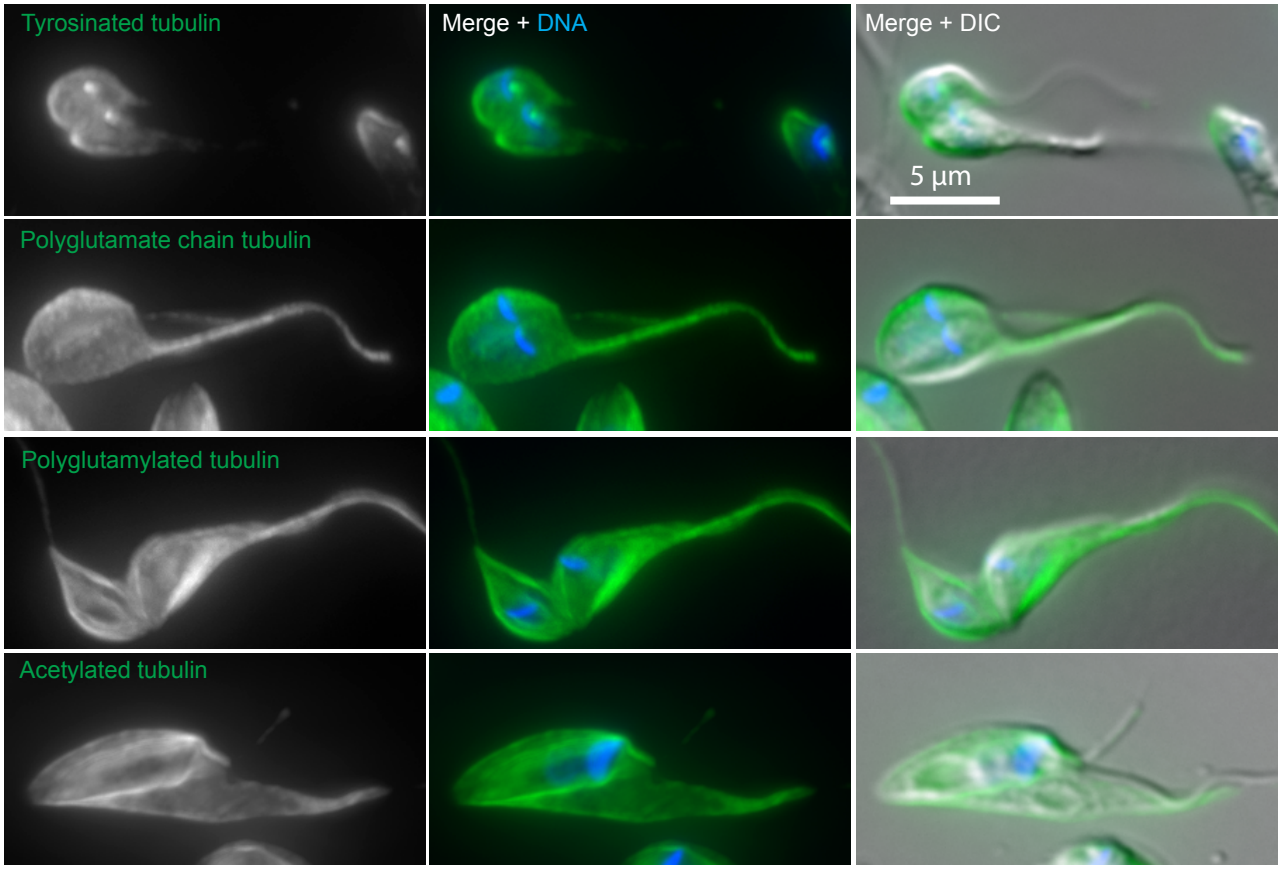
Tyrosinated tubulin
Merge + DNA
Merge + DIC
5 µm
Polyglutamate chain tubulin
Polyglutamylated tubulin
Acetylated tubulin

S1 Fig

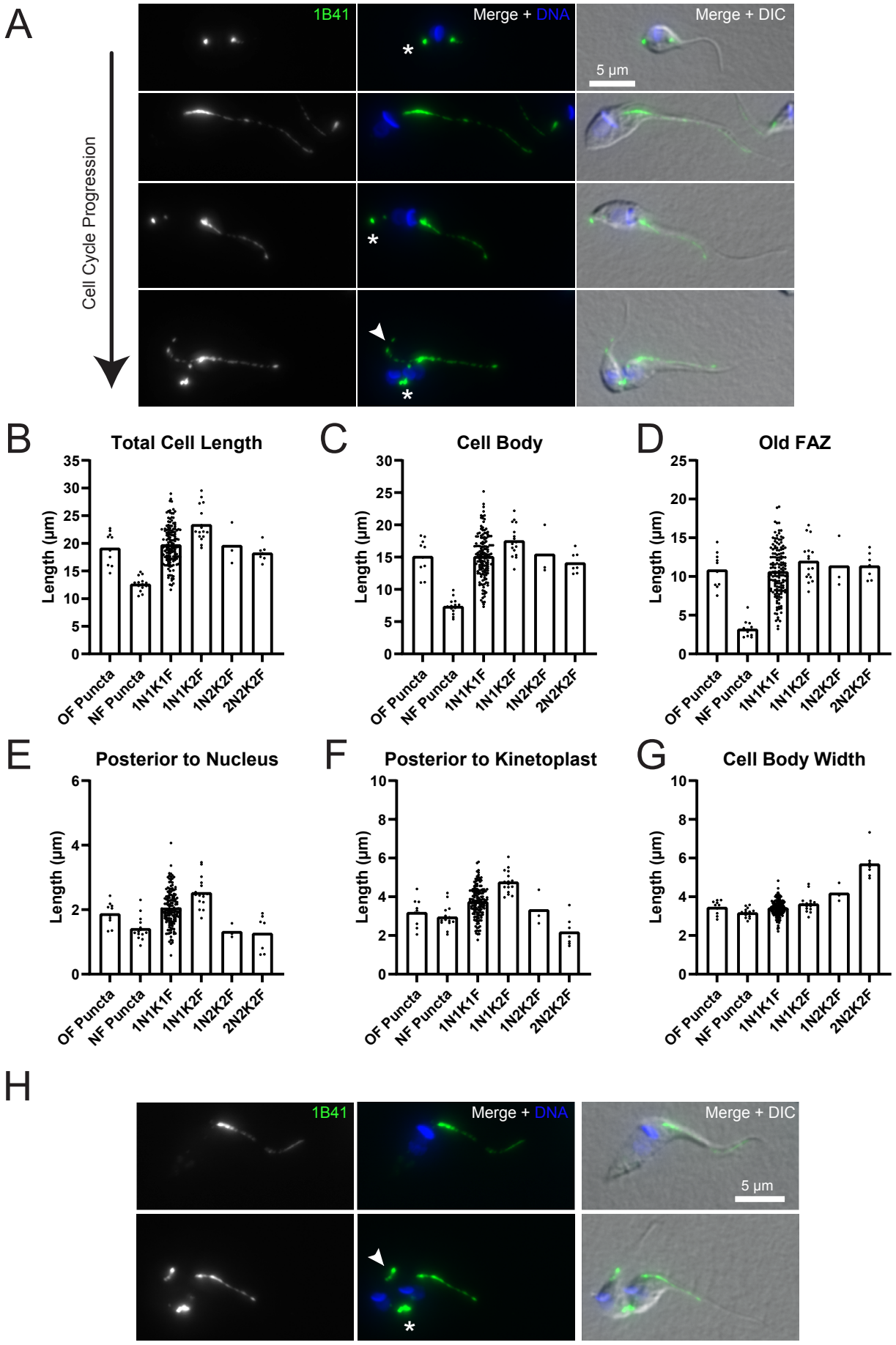
A
1B41
Merge + DNA
Merge + DIC
5 µm
Cell Cycle Progression
B
Total Cell Length
C
Cell Body
D
Old FAZ
E
Posterior to Nucleus
F
Posterior to Kinetoplast
G
Cell Body Width
Length (µm)
OF Puncta
NF Puncta
1N1K1F
1N1K2F
1N2K2F
2N2K2F
H
1B41
Merge + DNA
Merge + DIC
5 µm

S2 Fig

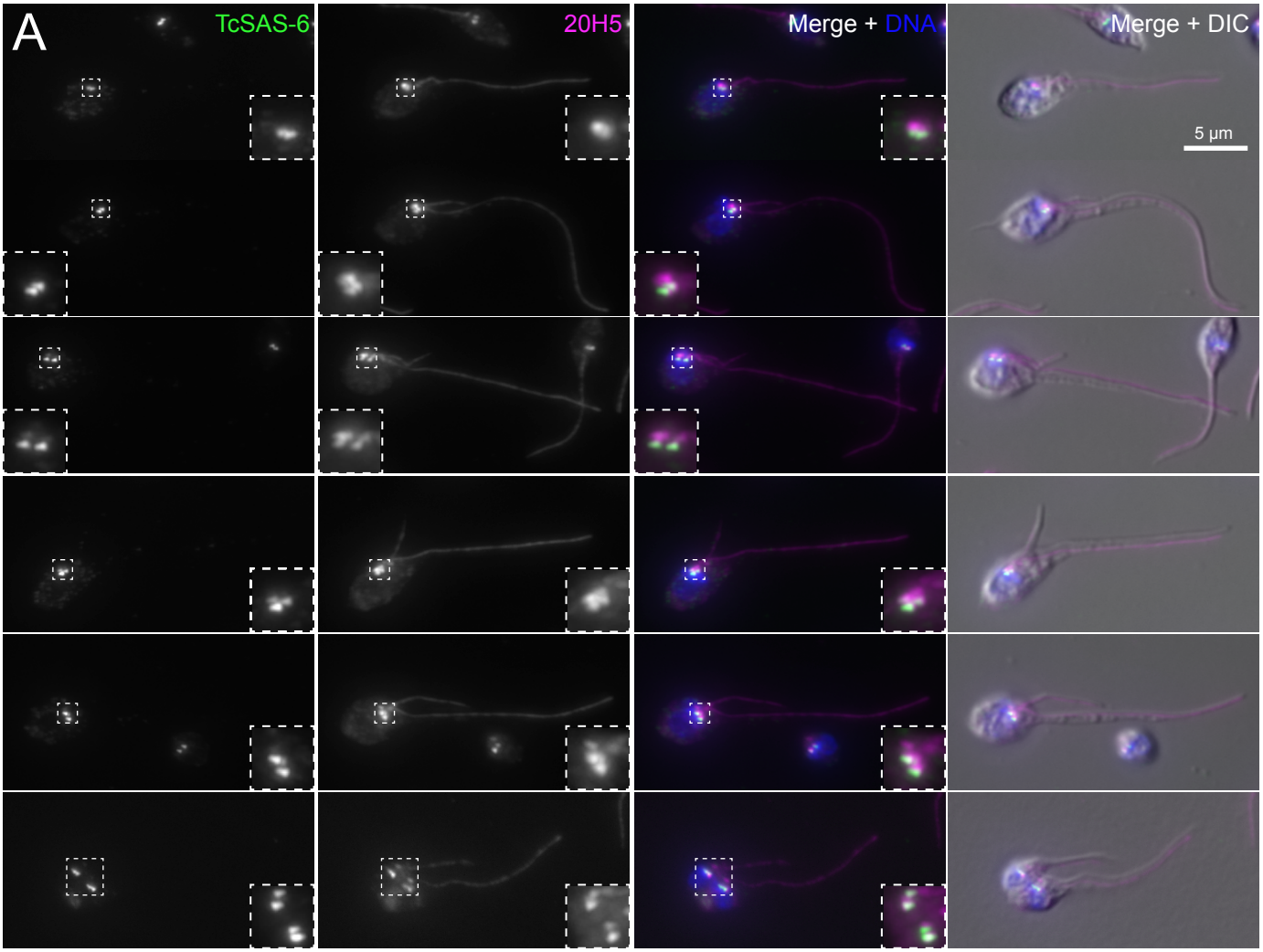
A
TcSAS-6
20H5
Merge + DNA
Merge + DIC
5 µm

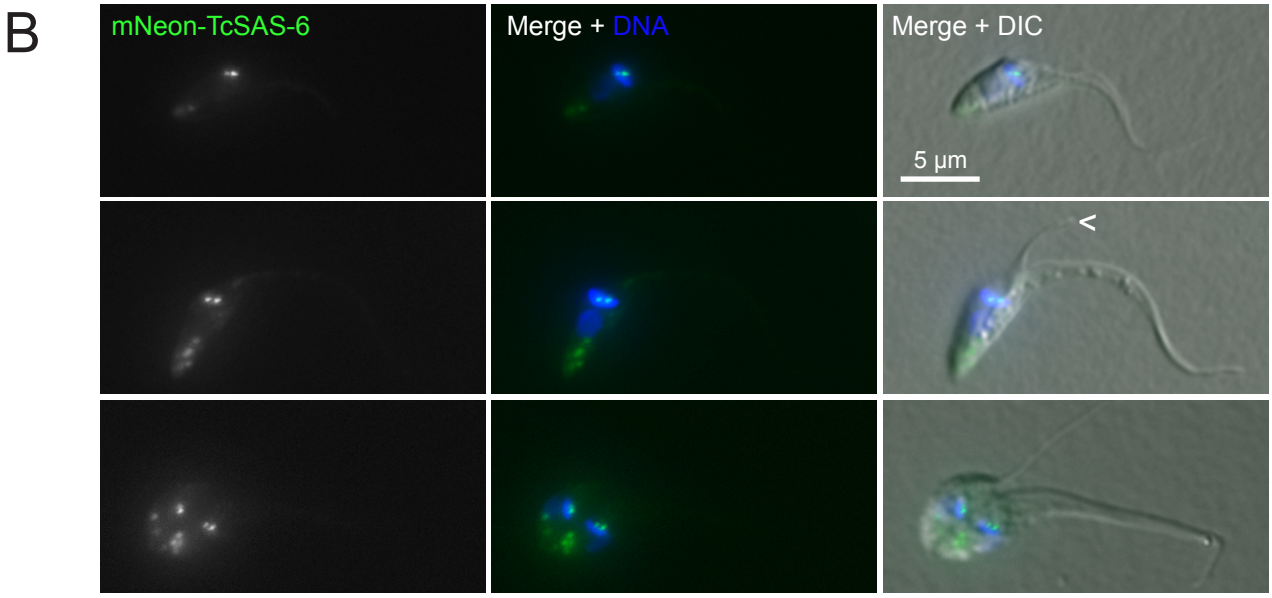
B
mNeon-TcSAS-6
Merge + DNA
Merge + DIC
5 µm
<

S3 Fig

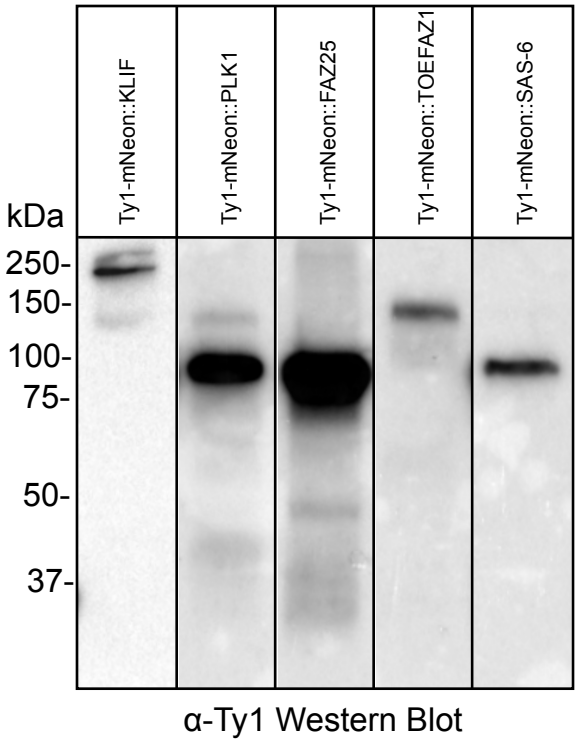
Ty1-mNeon::KLIF
Ty1-mNeon::PLK1
Ty1-mNeon::FAZ25
Ty1-mNeon::TOEFAZ1
Ty1-mNeon::SAS-6
kDa
250-
150-
100-
75-
50-
37-
α-Ty1 Western Blot

S4 Fig